Exploration of Neuroprotective Therapy

Open Exploration

Open Access Original Article

Redefining post-stress depression as a spatiotemporal five-disease multimorbidity trajectory: ghrelin-driven anchoring by Shugan absorbed compounds

Xi Huang[†*], Runze Zhou[†], Chendong Xu, Haotian Qian, Yunke Huang, Zhan Gao, Qiulong Zhao, Min Xu, Shaoqi Shi, Ailing Yu, Jialing Zhou, Yaling Liu, Chenxiao Shan, Ping Ren

Institute of Comorbid Depression, Nanjing University of Chinese Medicine, Nanjing 210023, Jiangsu Province, China

[†]These authors contributed equally to this work.

***Correspondence:** Xi Huang, Institute of Comorbid Depression, Nanjing University of Chinese Medicine, NO. 138 XianLin Avenue, QiXia District, Nanjing 210023, Jiangsu Province, China. 290606@njucm.edu.cn

Academic Editor: Guanghui Wang, Soochow University College of Pharmaceutical Sciences, China

Received: December 8, 2025 **Accepted:** April 29, 2026 **Published:** June 25, 2026

Cite this article: Huang X, Zhou R, Xu C, Qian H, Huang Y, Gao Z, et al. Redefining post-stress depression as a spatiotemporal five-disease multimorbidity trajectory: ghrelin-driven anchoring by Shugan absorbed compounds. Explor Neuroprot Ther. 2026;6:1004159. https://doi.org/10.37349/ent.2026.1004159

Abstract

Aim: This study aimed to redefine post-stress depressive pathogenesis through a novel five-disease multimorbidity trajectory model (brain$_1$-coronary-brain$_2$-gastro-enteric; B_1CB_2GE) and to evaluate the multifunctional anchoring effects of *Bupleurum chinense* Shugan-San (BSS) and its absorbed compounds (ACs), including meranzin hydrate (MH), in AFS (acute forced swimming) male Sprague-Dawley rats.

Methods: Temporal multimorbidity trajectories of B_1CB_2GE clusters were established in AFS rats and compared with single-disease models using 10 integrative analytic methods, including dynamic cluster trajectory modeling, biochemical profiling, and pharmacokinetic-pharmacodynamic (PK-PD) correlation analyses. A multi-cell experiment was used as a proxy for the in vivo system, whereas H-ECs (H_2O_2-treated endothelial cells) were used as a proxy for the multicellular system. Circulatory biomarkers related to oxidative, endothelial, and inflammatory (OEI) impairment, brain-derived neurotrophic factor (BDNF) levels, and cecal butyrate contents were measured. The role of the ghrelin (Ghr) receptor was examined using the antagonist D-Lys3-GHRP-6 (D-Lys). Forced-swim test, gastric emptying, enteric transit, and coronary flow were used to characterize post-AFS multimorbidity trajectory phenotypes in animals.

Results: Fifteen minutes after AFS, distinct temporal B_1CB_2GE multimorbidity clusters emerged with normalized ranking values: G 15.31 > B_2 1.17 > B_1 0.85 > C 0.49 > E 0.32. These clusters were accurately anchored by BSS and its five tailored sets of 1–10 ACs, demonstrating multifunctional modulation ranging from 53.23% to 156.32%, with optimal anchoring efficiency of 96.37–104.14%. MH, a representative multifunctional compound, exhibited the strongest prokinetic and OEI-restorative effects, elevating BDNF and cecal butyrate levels. These therapeutic effects were abolished by D-Lys, confirming a Ghr-dependent mechanism.

Conclusions: This study introduces a multimorbidity trajectory framework (B_1CB_2GE) for modeling post-stress depression and demonstrates that Shugan-like herbal formulas such as BSS effectively anchor

dynamic multimorbidity progression via multifunctional compounds like MH. These findings provide a systems-pharmacology basis for understanding and treating complex comorbid depressive disorders through multifunctional anchoring herbal therapeutics.

Keywords

temporal multimorbidity trajectory, acute forced swim, normalization animal model, multifunction

Introduction

To develop a Shugan-like multifunctional tool for anchoring multimorbidity trajectories, we introduced a new strategy called bioethnopharmaceutical analytical pharmacology (BAP), wherein we elucidated three representative absorbed compounds (ACs) contributing 97.56% to cardio-protection of the five-herbal GXII (Guanxin II) [1] within 3 years, a significant improvement compared to the century-long historical use owing to the method's efficiency, in which the number of ACs detected post-dose was much lower than the 32 compounds detected in GXII decoction in vitro (https://tcmsp-e.com/tcmsp.php). Additionally, using BAP [2], we elucidated that the contribution rate (CR) of 8 pharmacodynamic substances from *Fructus aurantii* & *Magnolia Bark* was multifunctional (81.25–120.43%), including 11 indices of antidepressive, gastro-enteric prokinetic (AGE), anti-inflammatory, and antioxidant [3]. The contribution of AGE as a multi-phenotype-based ranged from 98.23% to 103.45%. However, some invalid ACs were not eliminated during the three-year research period (the duration of a typical Chinese Ph.D or M.S. program), including 10 multifunctional ACs derived from the seven-herb formula of *Bupleurum chinense* Shugan-San (BSS) [4]. Conducting an in vivo experiment for all possible AC groupings is time-consuming and exceeds the practical limits of any research team.

Interestingly, the recently developed BAPevive (bioethnopharmaceutical analytical pharmacology: ex vivo to in vivo) approach—combining Bioavailability Prediction (BAP) with ex vivo-to-in vivo extrapolation—effectively removed invalid and redundant ACs by applying an interference-free post-dose supernatant of deproteinized serum (PSDS) derived from the traditional Chinese medicine Lianhuaqingwen (LH), in which equivalent doses for patients with COVID-19, rat mimic models, and relevant ex vivo systems were established using a patient-to-rat dose conversion coefficient and the ratio of rat in vivo dose to blood volume to estimate an ex vivo equivalent dose relevant to bioavailability. The resulting LH-PSDS profile closely matched the in vivo circulatory profile of LH post-dose, effectively eliminating 17–29% of false ex vivo responses that occurred when LH was added directly [4]. To date, the number of publications involving false responses to crude herbal extracts and post-dose serum have reached 252,134 and 6,059, respectively (2026/3/11 from PubMed). Despite longstanding criticisms of inconsistent results derived from methods using herbal extracts or serum that do not reflect in vivo circulation since 2014 [5], the number of such studies has continued to rise—from 6,624 and 289 papers in 2014 to 11,946 and 362 in 2023, representing increases of ~80.34% and 25.26%, respectively. Furthermore, within six months, the BAPevive approach, applied to endothelial nitric oxide (eNOS), nitric oxide (NO), and reactive oxygen species (ROS) in H_2O_2-treated endothelial cells (H-ECs) and healthy rats, successfully extrapolated the pharmacological roles of syringic acid and ferulic acid (FA). This was achieved after removing three invalid ACs, using mono-botanical grape extract as a proxy for 94.57% mono-functional endothelium-dependent (E+) coronary flow-mediated dilation (CFMD), i.e., coronary flow (CF) or vasodilation (< 6% difference with ex vivo 88.65%), implicating anti-oxidative sensitivity and an increase in NO bioavailability of the Src-PI3K/Akt-eNOS pathway (Src-phosphatidylinositol 3-kinase/protein kinase B-eNOS synthase) [5].

Acute forced swimming (AFS) is a widely used paradigm for evaluating antidepressant efficacy. A higher-intensity AFS challenge (15 min) induced depression-like phenotypes in rats, supporting its application in integrated disease–drug research. Over the past 14 years, we have repeatedly validated the primary functions of AGE induced by Shugan (BSS), its components, and its active compounds (ACs), through nine experimental replications. These experiments targeted temporally fixed disease clusters—specifically, depressive-like behavior and gastroenteric hypomotility (BGE)—by activating key biological

mechanisms such as the glutamatergic system, AMPAR (α-amino-3-hydroxy-5-methyl-4-isoxazolepropionic acid receptor), BDNF (brain-derived neurotrophic factor), mTOR (mechanistic target of rapamycin), synapsin I, ghrelin (Ghr) signaling, gastrointestinal NO synthase, anti-inflammatory and antioxidant pathways, monoaminergic systems, the HPA (hypothalamic-pituitary-adrenal) axis, the α_2-adrenoceptor pathway, and gastric emptying (GE)-peptide regulation in AFS rats [3, 6–11]. However, previous BAP/BAPevive studies mainly focused on one-source or two-source absorbed-compound analyses [4, 5, 12], whereas the temporal trajectories of Shugan-like multifunction-anchored disease clusters beyond BGE and their extension to seven-herb BSS with five function/morbidity-related readouts remain unclear. In the present study, this strategy was further extended from the previously identified 10 ACs to four sets of ACs derived from the BSS formula. As illustrated in Figure 1, we summarized the dysregulation and dysfunction observed across different organs into a multi-disease cluster. In this framework, impairments occurring in a single organ or function are defined as single diseases, whereas the aggregation of multiple single diseases within an individual constitutes a multi-disease cluster.

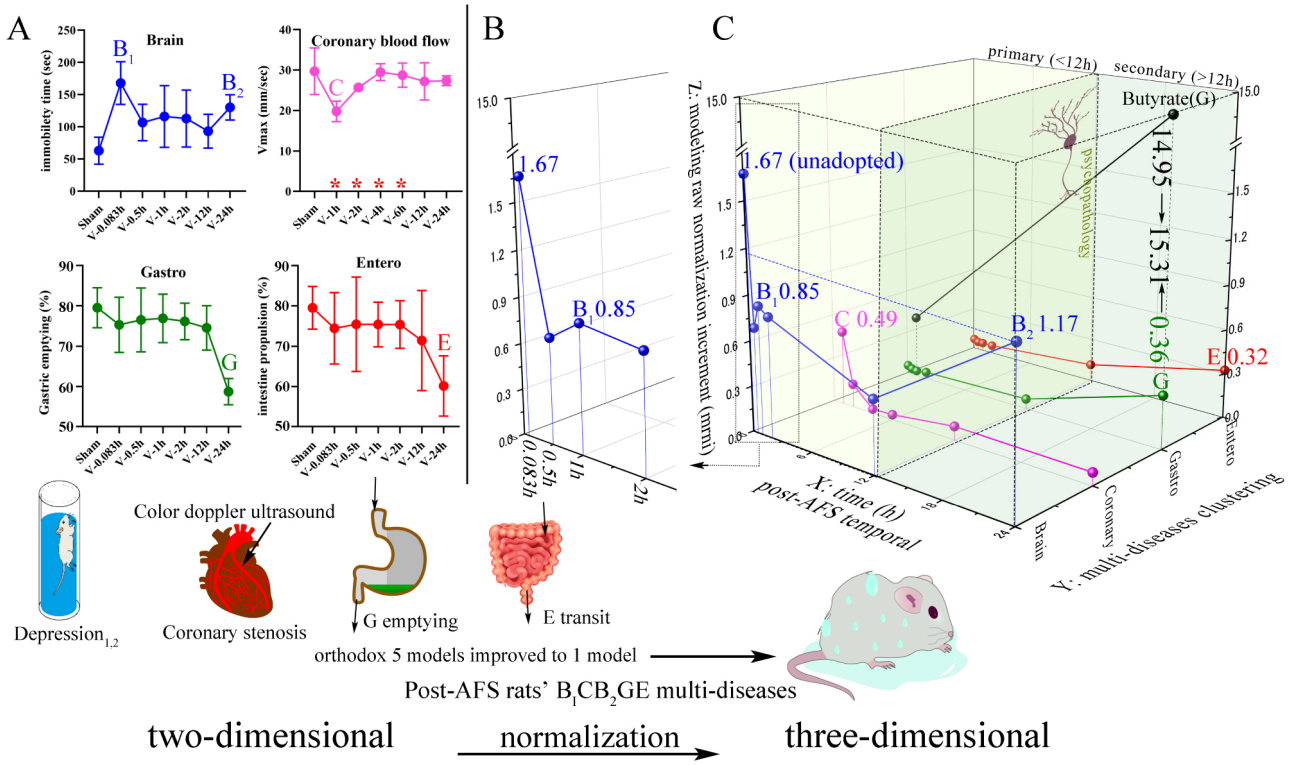

Figure 1. The integrated figure shifts from two to three dimensions (4 graphs to 1) in AFS rats with temporal B_1CB_2GE five disease clusters via comparable model raw normalization increment (mrni). (**A**) Separated B_1CB_2GE ($Brain_1$, Coronary, $Brain_2$, Gastro, Entero) 5 diseases in 4 different organs/dimensional graphs (whose brain contained 2 different depressions as B_1 and B_2 in the upper left) from post-AFS rats, both using raw data and expressed by traditional two-dimensional graphs. Orthodox graphs of disease-model are isolated, i.e., one disease/per graph; our one graph contained 5 diseases in one AFS model. The red asterisks mark differences on the x-axis. (**B**) The enlarged part of the brain (depression) from 0.083 h to 2 h in order to clearly show mrni at different times. (**C**) Three-dimensional (X-, Y-, and Z-axes) graphs from the shift of the former two dimensions of B_1CB_2GE (B_1 is + depressed brain 1 h post-AFS, i.e., mild depressive behavior, B_2 is ++ depressed brain, i.e., severe depression 24 h post-AFS, C is coronary flow, i.e., VTI as a biomarker of myocardial ischemia of ischemic heart disease, GE is functional gastric emptying disorders, consensual reducing ↓ gastric emptying and ↓ intestinal transit. B_1 and B_2 are what we described as primary and secondary depression, which are separated by psychopathology. Under the situation of lacking unique comprehensive biological model, this three-dimensional graph accesses broader data and includes different clusters of multiple conditions, helping us demystify multimorbidity at different stages of life. The X-axis: temporal 12 h as boundary marker, the former 0, 0.083, 0.5, 1, 2 and 6 h post-AFS as primary multimorbidity datum relevant to direct, fasting-act, short and last responses to single-use stress AFS during 0.083–1 h, and positive gut flora not shown during 0.083–12 h, and the latter 24 h (18 h is negative) as secondary multimorbidity data. The Y-axis is temporal clusters post-AFS of 1 h B_1C and 24 h B_2GE. Z-axis is mrni, i.e., modeling raw normalization increment. AFS: acute forced swimming; VTI: velocity-time integrals.

Herein, we propose a hypothesis: by using a rapid, precise, and cost-effective BAPevive strategy along with a Ghr-driven super-regulation network (SRN), we can eliminate many invalid ACs, thereby reducing

the time-intensive nature of in vivo grouping and making previously unfeasible in vivo animal experiments possible. Initially, we can extrapolate several representative sets of ≤ 10 ACs from 1,250 monomers (source: https://old.tcmsp-e.com/tcmsp.php) as a proxy for the seven-herb BSS formula in modeling the time-dependent AGEV (antidepressive-gastroenteric prokinetic-vasoactive) multifunction. Subsequently, post-stress temporal multi-functional ACs can be accurately docked to anchor multimorbidity trajectories. i) We aim to improve the BAPevive strategy by identifying any invalid compounds among the 10 multifunctional ACs derived from BSS. ii) If such compounds are identified, we will eliminate them to obtain multiple sets of multifunctional ACs that replicate the effects of BSS. iii) We aim to tailor a tool based on AGEV-like five-function ACs to anchor temporal trajectories of five disease clusters, characterized by increased immobility time, decreased gastric emptying, intestinal transit (IT), and decreased E+ CFMD. iv) Four graphs (one of which includes two depressions labeled B_1 and B_2), representing two-dimensional models of five diseases, are integrated into a single three-dimensional graph (Figure 1A and C). v) We elucidate the shared Ghr-driven SRNs through D-Lys, identifying them as the most potent and comprehensive inhibitors of the strongest monomer-induced multifunctional effects among the nine D-Lys-containing multifunctional inhibitors.

Materials and methods

Drugs

The seven herbs (Radix Bupleuri, Pericarpium Citri Reticulatae, *Ligusticum Wallichii*, Radix Paeoniae Alba, Rhizoma Cyperi, *Fructus Aurantii*, and *Glycyrrhiza uralensis Fisch*; the ratio of which is 4:4:3:3:3:3:1) constituting BSS were purchased from the Department of Pharmacy of Xiangya Hospital of Central South University and authenticated by the herbal medicine botanist Professor Hu, Z.H., Nanjing University of Chinese Medicine. The original herbs were kept at the Institute of Common Disease and Depression, Nanjing University of Chinese Medicine, China. Meranzin hydrate (MH) ($C_{15}H_{18}O_5$, CID, 5070783; Lot, 5673-37-0) supplied by DIAO (Chengdu, China) was greater than 98% pure. Albiflorin ($C_{23}H_{28}O_{11}$, CID, 24868421; Lot, MUST-19041601), FA ($C_{10}H_{10}O_4$, CID, 445858; Lot, MUST-19032928), Naringin ($C_{27}H_{32}O_{14}$, CID, 442428; Lot, MUST-18050808), Hesperidin ($C_{28}H_{34}O_{15}$, CID, 10621; Lot, MUST-19030701), Glycyrrhizic acid ($C_{42}H_{62}O_{16}$, CID, 14982; Lot, MUST-19052407), Saikosaponin A ($C_{42}H_{68}O_{13}$, CID, 167928; Lot, MUST-19101401), Nobiletin ($C_{21}H_{22}O_8$, CID, 72344; Lot, MUST-19041210), Tangeretin ($C_{20}H_{20}O_7$, CID, 68077; Lot, MUST-18012910) and Glycyrrhetinic acid ($C_{34}H_{50}O_7$, CID, 10114; Lot, MUST-19032207) with ≥ 98% purity were obtained from Chengdu Must Bio-technology Co., Ltd. (Chengdu, China). HPLC/MS grade methanol, acetonitrile, and formic acid (CNW, USA) were used for the analysis. Deionized water purified by the Milli-Q system (Millipore, Billerica, MA, USA) was available. [D-Lys3]-GHRP-6 was received from Abcam Co, Cambridge, England, UK. DMSO, phenylephrine hydrochloride (PE), acetylcholine (Ach) chloride, WAY100635, NBQX, SB207266 and NG-nitro-*L*-arginine methyl ester (L-NAME) were produced by Sigma-Aldrich Co. St. Louis, MO, USA. During cell culture procedures, DMEM (Hyclone, USA), pancreatin digest (Hyclone, USA), fetal bovine serum (FBS) (Gibco, USA) and penicillin-streptomycin solution (Beyotime, Shanghai) were used.

Preparation of BSS, the BPSDS

The extraction of BSS was performed as described in our previous study [13]. Briefly, the seven herbs were mixed, soaked in 10-fold volumes of water for 30 min, refluxed twice for 30 min, and filtered to obtain the combined extract. Whereafter the blended liquid was concentrated, frozen rapidly, and dried in a freeze-dryer (Labconco, USA). The yield of lyophilized powder (BSS for short) was 27.80%.

BPSDS was prepared as follows. After 45 minutes of intragastrically administering 30 $g \cdot kg^{-1}$ BSS or an equal dose of normal saline to rats [6], blood was collected from the accessory aorta of anesthetized rats and processed to obtain BSS post-dose rat serum (PRS) or blank serum (BS) by centrifuging at 3,500 rpm for 10 min. Afterwards, 200 μL of purified water was added to 1 mL of CMS or BS, mixed for 2 min, and placed in boiling water for 5 min to precipitate the protein. Then we homogenized the sample by grinding

at 30 Hz for 2 min, centrifuged at 12,000 r min^{-1} for 15 min at 4°C. The supernatant was transferred to another clean vial, forming BPSDS as one of the herbal ex vivo proxies. Another proxy was the previously mentioned representative herbal ACs.

Experimental animals

Sprague-Dawley rats (male, 220 ± 20 g) were purchased from Nanjing Qingzilan Technology Co., Ltd. All animal welfare and experimental procedures carried out were consistent with the guide for the Care and Use of Laboratory Animals approved by the Institutional Animal Care and Use committee at Nanjing University of Chinese Medicine (a 12 h light/dark cycle, 23 ± 2°C, and 60 ± 5% relative humidity). After acclimatizing to the surroundings for seven days, the rats were randomly divided into groups.

The rats (n = 6) got the intragastrical administration of BSS (30 g·kg^{-1}) and other drugs before narcosis through intraperitoneal injection of 3% pentobarbital sodium (30 mL·kg^{-1}). Then, rats were euthanized by drawing blood from the abdominal aorta. All animal experimental procedures were performed in accordance with the Guide for the Care and Use of Laboratory Animals approved by the Institutional Animal Care and Use Committee at Nanjing University of Chinese Medicine (Resolution No. 201912A008).

Qualitative and quantitative determination of 10 ACs in BSS and serum

A chromatographic separation was conducted on the Waters ACQUITY BEH C18 column (2.1 × 100 mm, 1.7 μm) maintained at 35°C. The mobile phase comprised 0.1% formic aqueous solution (A) and acetonitrile solution (B) at a gradient program as follows: 0.0–1.0 min, 10% B; 1.0–3.5 min, 10–20% B; 3.5–5.5 min, 20–26% B; 5.5–21.0 min, 26–95% B; and 21.0–25.0 min, 95% B. The flow rate was set at 0.4 mL/min, and the injection volume was 2 μL.

MS data were acquired using the Waters Xexo G2-XS QTOF system (Waters, USA) equipped with an electrospray ionization (ESI) source. The ionization voltage was set at 1 kV. Other parameters were set as follows: source offset, 50 L/h; source temperature, 120°C; desolvation temperature, 450°C; and desolvation gas flow rate, 800 L/h. Analyte detection was carried out using MRM in a positive mode. The precursor-to-product ion transitions, acquisition duration, con voltage (Con), and collision energy were shown in Tables S1 and S2. Relevantextract ion flow chromatograms of 10 ACs in mixed reference solution (A) and BSS decoction sample (B) and internal standard (IS) were shown in Figure S1.

Calculating compound doses

Various doses of BSS (32.58, 65.16, and 130.30 mg/mL) were designed as ex vivo doses for isolated aortic baths or H-ECs. The present and previous 30 g/kg [13] single in vivo BSS doses were multiplied by the coefficient of 0.25 to determine the polyphenol doses for rats (0.25 kg) as 7.5 g. Next, the above total dose (7.5 g) following complete absorption (100% bioavailability) was divided by the blood volume (16 mL for rats, respectively) to obtain 468.75 mg/mL of blood, similar 100% bioavailability. The 468.75 mg/mL blood was multiplied by the yield of lyophilized powder (27.80%) to acquire an in vitro dose of 130.30 mg/mL crude extract in blood. Thus, the ex vivo dose (mg/L) of BSS at 32.58 mg/mL and 65.16 mg/mL equaled ~25% or ~50% bioavailability. And according to the above calculation, the L-, M-, and H-doses of BPSDS in rats were designated as 7.5, 15 and 30 g/kg. Our ACs each ex vivo and in vivo doses equated their contents in PRS and BSS.

NO, eNOS and ROS in ECs

Sprague Dawley rat aortic ECs were provided by Procell Life Science & Technology Co., Ltd. and cultured in DMEM supplemented with 10% FBS + 1% penicillin/streptomycin. The medium was replaced every two to three days. We performed the cell passage when the confluence of cells reached about 80% and digested the cells using trypsin. Rat aortic endothelial cells (RAECs) were cultivated in 96-well plates, washed with phosphate-buffered saline (PBS) three times, and incubated at 37°C for 24 h. Then ECs were stimulated as a cellular model of oxidative stress by incubating with 0.5 mM H_2O_2 for 12 h. BPSDS, 10 ACs, alone or in

different mixes whose dose equals the determined content in serum, as shown in Table 1, were added into the culture medium 45 mins before adding H_2O_2. The cell supernatant was collected, and the levels of eNOS and NO were detected using colorimetry and ELISA kits, while the ROS level was detected by flow cytometry. Relevant results are shown in Tables 1 and 2.

Establishment of multiple cell models

Rat brain microvascular endothelial cells (BMECs): Cells were isolated from postnatal day 7–14 (P7–P14) Sprague-Dawley (SD) rat pups of SPF grade, without distinction of sex. Rat hippocampal microglia (HM): Cells were obtained from postnatal day 1 (P1) Sprague-Dawley (SD) rat pups of SPF grade, without distinction of sex. Rat hippocampal neurons (HN): Cells were prepared from postnatal day 1 (P1) Sprague-Dawley (SD) rat pups of SPF grade, without distinction of sex. Rat HN, HM and BMECs were isolated, purified and cultured according to the method of neurovascular unit (NVU). After seeding neurons into six-well culture plates for 3–5 days, purified astrocytes were seeded to the outside of the well inserts, and then the well inserts were placed into the corresponding six-well culture plates. After 1 day of co-culture, purified BMECs were seeded to the inner side of the well inserts, and the NVU was successfully established. Specific markers such as neuron-specific enolase, glial fibrillary acidic protein and platelet adhesion molecule-1 (CD31) were used to identify HN, HM and BMEC. After treatment with 200 μM corticosterone for 18 h, MH treatment was given for 45 min to establish the cell model. The levels of 5-HT (5-hydroxytryptamine), BDNF and IL-6 (interleukin-6) were measured using the appropriate kits.

10^5 gastric smooth muscle cells and 400 μL complete medium were added to sterile centrifuge tubes and incubated at 37°C for 24 h, followed by a 45-min MH treatment. Ach at a final concentration of 0.1 μM was then added to each tube for 10 min for detection. MCP-1 (monocyte chemoattractant protein-1), ET-1 (endothelin-1), and IL-6 levels were measured using the appropriate kits.

Forced swimming test (FST)

In the previous study [3, 8], we have evaluated the antidepressant effect through FST, which was described by Porsolt et al. [14]. The rats were randomly divided into group with 8 rats in each group. Rats were individually forced to swim twice at 24 h intervals in a vertical glass cylinder (40 cm high, 18 cm in diameter) filled with water (25 ± 2°C) up to 30 cm. On the first day, each rat was subjected to a pre-swimming for 15 min to induce the AFS model. The immobility time in 5 min was measured by putting the rats into the same glass cylinder individually, 30 min after administration. All conductors were arranged from 9:00 a.m. to 11:00 a.m. The water was changed between the two trials. The rats were considered immobile when they showed behavior of floating motionlessly or merely making actions to prevent drowning through the TopScan Version 3.0 software.

Changes in velocity-time integrals (VTI) by BPSDS vs. absorbed ACs

The left anterior descending coronary artery (LAD) diastolic flow VTI were achieved by analyzing and detecting the diastolic phase of the Doppler signals and parameters using image analysis software to evaluate CF. The Vevo 2100 system (Visual Sonics, Toronto, Canada) was used to perform all ultrasound exams to establish their in vivo bioactive link and to further study BSS-induced vasodilation. Each rat was given 3% inhalant isoflurane for anesthesia, and maintained with 1.0–1.25% isoflurane in oxygen-enriched air (30% oxygen/70% air) with spontaneous ventilation. The hair of the rats' chest walls was carefully removed, and the chest wall was smeared with ultrasonically coupled fluid for ultrasound imaging examination. VTI is often used as a typical indicator of CF or CFMD.

Changes in vascular tension by BPSDS vs. absorbed ACs

The thoracic aortas were quickly separated out from the anesthetized rats and then placed in a precooled dissecting tray filled with Krebs-Henseleit (K-H) buffer [the composition (mM) of which is NaCl 119, KCl 4.7, $CaCl_2$ 2.5, KH_2PO_4 1.2, $MgSO_4$ 1.2, $NaHCO_3$ 25, glucose•H_2O 11, and EDTA-2Na 0.5, pH 7.4] at 37°C. The vascular rings, latch onto which the tissue and fatty tissue were removed, were cut into small pieces

Table 1. Differences in the contribution of ACs to the multifunction of BPSDS (P) and BSS (B) in 1st standard or 3rd validation evive in multi-cells and/or 2nd rapid ECs-shared AFS rats in vivo using multifunctions comparing ACs {dose = their contents in P and B, calculation by [(ACs – V) – (V – S)] ÷ [(B or P – V) – (V – S)]} and P or B calculation by (D – V) ÷ (V – S).

Ex vivo grouping Group/Contribution/Difference Equation/Group			[(ACs – V) – (V – S)]/[(B or P – V) – (V – S)] (D – V)/(V – S)				Ex vivo-to-in vivo extrapolation: Contribution (%)				Difference (%) comparison of 1st–2nd or 2nd–3rd
			Sham (S)	Vehicle (V)	ACs	BPSDS (P)	Multi-cell (%)	[#] In vivo (%)		Rapid ECs (%)	
Aorta ECs	Standard	10 ACs	42.67 ± 0.36	71.11 ± 0.04	44.61 ± 0.04	42.96 ± 0.01	ET-1: 96.62	Coronary flow (mm)	96.37	NO: 97.78	1.16
	Validation	HS			50.69 ± 0.48		ET-1: 86.93		87.39	NO: 94.82	6.97
Gastric primary smooth muscle cells (GSMCs)	Standard	10 ACs	19.32 ± 0.58	1.17 ± 0.70	13.97 ± 0.70	11.25 ± 0.70	Contraction: 109.64	Gastric emptying (%)	153.06	NO: 97.78	11.86
	Validation	MF			10.13 ± 0.47		Contraction: 96.03		76.97	ROS: 100.09	4.06
GSMCs+ MCP-1	Standard	10 ACs	40 ± 0.74	174.21 ± 3.74	125.99 ± 1.12	100.56 ± 0.75	MCP-1: 87.77	Enteric transmit (%)	114.10	NO: 97.78	10.01
	Validation	HST			119.20 ± 3.43		MCP-1: 91.03		98.72	eNOS: 90.14	0.87
Brain: primary neurovascular unit (NVU)	Standard	10 ACs	0.39 ± 0.01	0.03 ± 0.01	0.19 ± 0.05	0.26 ± 0.02	BDNF: 88.14	Immo-bility (s)	91.43	eNOS: 88.19	3.24
	Validation	MF	7.22 ± 0.19	1.26 ± 0.02	3.58 ± 0.04	3.44 ± 0.02	5-HT: 101.72		104.58	NO: 100.94	0.78

[#] In vivo (%): result was shown in Table 2; 1st: standard in multi-cells (10 ACs); 2nd: rapid ECs-shared AFS rats in vivo using multifunctions comparing ACs; 3rd: validation in multi-cells (HS/MF/HST). ECs: endothelial cells; AFS: acute forced swimming; B: BSS (*Bupleurum chinense* Shugan-San); P: BPSDS; ACs: absorbed compounds; 5-HT: 5-hydroxytryptamine; BDNF: brain-derived neurotrophic factor; eNOS: endothelial nitric oxide; ET-1: endothelin-1; MCP-1: monocyte chemoattractant protein-1. Unit: ET-1 (pg/mL), contraction (%), MCP-1 (pg/mL), 5-HT (ng/mL), NO (μmol/L), eNOS (μmol/L), ROS (μmol/L).

3–4 mm in length. Soon afterwards, the vascular rings were individually fixed by two stainless steel hooks and placed in a 20 mL K-H buffer, continuously oxygenated with a gas mixture (95% O_2 and 5% CO_2) inside and heated by water outside. One hook was attached to the bottom of the bath, and the other was connected to the isometric transducer (model MLT0420, AD Instruments, Sydney, Australia). Then we acclimatized the rings to the in vitro environment preloaded with 1,000 mg for 1 h, until the contractility was stable. The contractility was recorded and analyzed in a monitor using Power Lab software (https://www.adinstruments.com/products/powerlab-daq-hardware). The K-H buffer was replaced to wash every 15 min during stabilization. The vascular activity was verified by stimulating the rings to obtain a reproducible shrinkage reaction with 60 mM KCl. Whereafter, we induced ≥ 80% vasodilation of rings constricted with 1 μM phenylephrine three times to bear out the function of the endothelium. After equilibrating for 30 min, we contracted rings by using phenylephrine again to curve the concentration relaxation curve of the ex vivo proxies, BSS, BPSDS, and ACs, alone or in combination. The doses of the components were consistent with their contents in serum.

Table 2. The contribution of multifunction induced by 10 ACs alone or in mixture to BPSDS via two normalization formulae calculations in H_2O_2-treated ECs.

Group/Formula		NO (μmol/L)	eNOS (μmol/L)	ROS (μmol/L)
Sham (S)		22.30 ± 0.22	37.20 ± 1.19	2,433.60 ± 41.88
Vehicle (V)		11.00 ± 0.52	17.53 ± 1.36	20,432.47 ± 411.95
BPSDS		20.76 ± 1.11	33.76 ± 2.26	7,652.73 ± 65.49
Contribution rate from 2 formulae	10 ACs	19.24 ± 1.39	29.52 ± 2.66	11,911.43 ± 70.90
	Formula 1 (%)	92.68	87.44	155.64
	Formula 2 (%)	97.78	88.19	86.16
	Hesperidin	23.50 ± 1.37	38.99 ± 1.07	2,804.47 ± 21.27
	F1	113.20	115.49	114.6
	F2	113.01	114.57	115.75
	Saikosaponin A	21.14 ± 1.81	41.18 ± 0.86	4,279.00 ± 126.90
	F1	101.83	121.98	55.91
	F2	101.80	120.67	110.96
	Tangeretin	20.55 ± 1.52	32.08 ± 1.25	5,904.83 ± 1.53
	F1	98.99	95.02	77.16
	F2	99.00	95.32	105.68
	Glycyrrhetinic acid	17.67 ± 0.88	29.39 ± 0.86	6,091.07 ± 58.66
	F1	85.12	87.06	79.59
	F2	85.33	87.83	105.07
	Albiflorin	15.59 ± 0.2	25.71 ± 0.86	6,433.73 ± 50.45
	F1	75.10	76.16	84.07
	F2	75.45	77.58	103.96
	Meranzin hydrate	18.13 ± 0.23	24.00 ± 0.11	11,328.17 ± 174.61
	F1	87.33	71.09	148.03
	F2	87.51	72.81	88.06
	Ferulic acid	16.96 ± 0.41	23.61 ± 0.71	15,090.63 ± 188.99
	F1	81.70	69.93	197.19
	F2	81.96	71.73	75.83
	Nobiletin	14.38 ± 1.24	21.09 ± 0.94	8,709.77 ± 70.91
	F1	69.27	62.47	113.81
	F2	69.71	64.71	96.57
	Naringin	12.91 ± 0.26	20.40 ± 1.09	10,501.00 ± 281.40
	F1	62.19	60.43	137.22
	F2	62.73	62.79	90.75
	Glycyrrhizic acid	8.75 ± 1.38	11.71 ± 0.51	12,978.40 ± 146.39
	F1	42.75	34.69	169.59
	F2	42.97	38.58	82.7

Formula 1: ACs/BPSDS; Formula 2: [(ACs – V) – (V – S)]/[(BPSDS or BSS – V) – (V – S)]. BSS: *Bupleurum chinense* Shugan-San; ECs: endothelial cells; eNOS: endothelial nitric oxide.

The effects on gastrointestinal motility in vivo

Motility was estimated by determining GE and IT. Firstly, each rat was forced to swim for 15 min to induce acute stress before gastrointestinal motility tests, and intragastrically administered with 1 mL Evans blue 30 min after drug administration (dissolved in 0.9% NaCl with 0.5% methylcellulose at the concentration of 50 mg/mL). The stomachs of euthanized rats were cut from the esophageal sphincter to the pyloric sphincter. The absorbance at 565 nm was determined with the Infinite M 200 Pro as previously reported by De Winter et al. [15].

The absorbance of Evans from rats in the control group was obtained immediately as a standard stomach control. The GE was acquired as follows:

$$GE\,(\%) = \frac{(A565\ reference\ -\ A565\ sample)}{A565\ reference} \times 100\%$$

Where:

"A565 reference" is the abbreviation of the absorbance of the reference stomach at 565 nm; "A565 sample" is the abbreviation of the absorbance of the sample stomach at 565 nm.

The IT was determined by measuring the distance travelled by the Evans blue from the pylorus and the total length of the small intestine. The IT was acquired as follows:

$$IT\,(\%) = \frac{Distance\ travelled\ by\ Evans\ blue}{Length\ of\ the\ small\ intestine} \times 100\%$$

Mechanism involved in AGEV polypharmacology

Fluoxetine (FLX), Ach, and mosapride (MOS) were added, respectively, into RAECs at 10 μM as relevant positive controls. Besides, to verify the relevant signaling path, the MF (MH + FA), HS (hesperidin + Saikosaponin A), and HST (HS + tangeretin) were chosen to separately emphatically explore the influence of suppressant, demonstrating their uniqueness and making way for the discovery of lead compounds. The 100 μM [D-Lys3]-GHRP-6 (the inhibitor of growth hormone secretagogue receptor, GHSR), 100 μM L-NAME (the inhibitor of eNOS), 100 μM PP2 (the inhibitor of Src), 100 μM WAY100635 (the inhibitor of 5-HT1A), 100 μM NBQX (the inhibitor of AMPA), and 100 μM SB-207266 (the inhibitor of 5-HT4) were added separately into RAECs 30 min before administration. In addition, the rats were injected with saline (1 mL/kg, s.c.) or relevant antagonists at a dose of 0.5 mg/kg 30 min before administration.

Statistical analysis

Data were shown as the mean ± SD and analyzed using GraphPad Prism 8.0 software (GraphPad Software, San Diego, California, USA, www.graphpad.com). For comparing multiple groups, one-way ANOVAs followed by *Q* tests were used. Comparisons between two groups were made using Student's *t*-tests. Statistical significance was assumed when $p < 0.05$.

To quantitatively compare different readouts from different tissues, organs and experimental levels, several normalization formula were used in this study. Model raw normalization increment (mrni) was used to indicate the deviation degree of the Vehicle (V)/model group from the Sham (S) group, with different formulas applied according to whether the V value was lower or higher than the S value. Drug raw normalization increment (drni) was used to evaluate the relative change produced by drug treatment on the basis of the V/model group. Phytochemical raw normalization increment (prni) was used to evaluate the relative effect and contribution of phytochemical/monomer treatment under the model background. On this basis, the CR was further calculated to estimate the relative contribution of a monomer or absorbed constituent to its parent herb/formula, and the rate of deviation (RD) was used to show the percentage difference between prediction and observation. These indices were introduced to reduce the fluctuation-related bias of raw values and to make comparisons among endpoints with different change directions and different magnitudes more homogeneous.

CR of monomer to parent herbs is calculated as follows:

$$CR\,(\%) = \frac{ACs\ -\ Sham}{Parent\ herbs\ -\ Sham} \times 100\%$$

RD of prediction to observation is calculated as follows:

$$RD\,(\%) = \left|\,1 - \frac{Prediction}{Observation}\,\right| \times 100\%$$

mrni formula is calculated as follows:

$$mrni = \begin{cases} \frac{(Sham - Vehicle)}{Vehicle}, & Vehicle < Sham \\ \frac{(Vehicle - Sham)}{Sham}, & Vehicle \geq Sham \end{cases}$$

drni formula is calculated as follows:

$$drni = \frac{Drug - Vehicle}{Vehicle}$$

prni formula is calculated as follows:

$$prni = \frac{Drug - Vehicle}{Vehicle - Sham}$$

Results

Temporal trajectories of five disease clusters

The ancient, multifunctional Shugan-guided BAPevive strategy [5]—after eliminating invalid compounds and correcting all orthodox database errors through normalization calculation—activates shared Ghr-driven SRNs in the Gan axis, enabling accurate tailoring of BSS's five sets of multifunctional AC tools within half a year, unlike previous BAP-alone methods that took three years to identify 8 out of 10 ACs, some of which were invalid [3, 4]. The identified AGEV ACs not only anchor the 24-h post-AFS depressed rat phenotype (B_2) but also uncover additional temporal trajectories—including 1-h B_1C and 24-h GE disorders—that constitute the full brain$_1$-coronary-brain$_2$-gastro-enteric (B_1CB_2GE) five-disease trajectory, previously overlooked by researchers. Furthermore, we used normalization-calculated herbal multifunctional ACs to anchor multimorbidity cluster dimensions, where the G mrni increased to 15.31—the highest among B_1CB_2GE clusters—corroborating epidemiological findings that poor appetite is a refractory root cause of depression-induced cardiac events. Thus, four graphs representing popular and orthodox two-dimensional models of five diseases (with B_1 and B_2 depressive behaviors grouped into one) were holistically integrated into a single, three-dimensional representation of B_1CB_2GE trajectories. The mrni ranking was: G 15.31 > B_2 1.17 > B_1 0.85 > C 0.49 > E 0.32 (Figure 1). Interestingly, for the first time to our knowledge, AFS rats and mice—including data from nine prior non-random, repeatable post-AFS AGE-3 disease rat [3, 4, 6–11, 16, 17] experiments and newly observed time-dependent depressive and coronary disorders—have been tailored as multimorbidity model frameworks homogeneously anchored by multifunctional ACs. From epidemiological surveys, we concluded that antidepressants (e.g., SSRIs, esketamine) increased the incidence of GE-hypomotility by 67%, along with heightened risks of hypertension, treatment discontinuation, and cardiac events [18–22]. These adverse effects were significantly reduced by the Shugan-like BSS and its five sets of ACs (Table 3).

Selected statistically positive time points (in h) and their post-AFS rankings—based on integrated non-random epidemiological incidence—were used as criteria to identify multimorbidity clusters. These included primary immobility (0.083–1 h; ranked 1, 3, and 4), along with E+ CFMD positivity from 1–3 h (other indices were negative), and secondary immobility at 24 h (ranked 2), which was the only time point showing GE hypomotility (Figure 1). The peak values of parallel immobility and isolated increases in E+ CF observed at 0.083–1 h post-AFS (ranked 1, 3, and 4) are considered primary BC clusters. In contrast, immobility at 24 h (ranked 2) and GE hypomotility observed only at 24 h are designated as secondary multimorbidity clusters, forming the temporal 1–24 h B_1C-B_2GE multimorbidity trajectories. During 13 years at different cities and universities, including the present (Figure 1), research groups have performed multiple repeatability tests of 24 h BGE [3, 6–11, 16, 17] (Figure 1) to 1–24 h B_1C-B_2GE cluster trajectories under nearly similar conditions of modeling, constituting stable non-random multimorbidity clusters traits in AFS rats, and found results highly consistent with epidemiological clustering of depression, cardiac events, and poor appetite, with roughly temporal relation from multimorbidity patients [21, 23].

Table 3. Ex/In vivo 4-functional contribution rate of ACs (A) alone or mixed with BPSDS or BSS via [(ACs – V) – (V – S)]/[(BPSDS or BSS – V) – (V – S)] calculating.

Group/Treatment	Ex vivo detection of H_2O_2-treated RAEC cells			Extrapolated value/% difference	In vitro detection of acute forced swim				
	NO (μmol/L) Mean ± SD Contribution	eNOS (μmol/L) Mean ± SD Contribution	ROS (μmol/L) Mean ± SD Contribution		VTI Mean ± SD Contribution	FST Mean ± SD Contribution	GE Mean ± SD Contribution	IP Mean ± SD Contribution	Error range %
S	22.30 ± 0.22	37.20 ± 1.19	2,433.60 ± 41.88	—	28.75 ± 5.08	82.60 ± 12.68	0.795 ± 0.053	0.793 ± 0.055	—
	—	—	—	—	—	—	—	—	—
V	11.00 ± 0.52	17.53 ± 1.36	20,432.47 ± 411.95	—	18.35 ± 1.63	179.63 ± 3.70	0.587 ± 0.106	0.601 ± 0.075	—
	—	—	—	—	—	—	—	—	—
BPSDS or BSS	20.76 ± 1.10	33.76 ± 2.26	7,652.73 ± 65.49	—	25.87 ± 5.85*	103.70 ± 5.56*	0.722 ± 0.073*	0.721 ± 0.037*	—
	—	—	—	—	—	—	—	—	—
MH	18.13 ± 0.23	24.00 ± 0.11	11,328.17 ± 174.61	NO 92.1%	21.20 ± 0.98	97.06 ± 25.92	0.882 ± 0.091	0.734 ± 0.052	—
	92.1%	72.81%	88.06%	eNOS 72.81%	73.94%	103.84%	146.65%#	104.14%	—
	—	—	—	Difference	1.13%	11.74%	54.55%	12.04%	1.13–12.04
FA	16.96 ± 0.41	23.61 ± 0.71	15,090.6 ± 188.99	NO 81.96%	28.07 ± 0.52	120.37 ± 10.37	0.729 ± 0.104	0.882 ± 0.046	—
	81.96%	71.73%	75.83%	—	112.28%	90.36%	102.04%	151.27%#	—
	—	—	—	Difference	30.32%	8.4%	20.08%	69.31%	8.4–30.32
MH + FA	20.96 ± 0.52	32.17 ± 0.70	7,683.34 ± 174.82	NO 100.94%	18.77 ± 19.71	95.77 ± 19.71	0.643 ± 0.014	0.650 ± 0.042	—
	100.94%	95.57%	100.09%	eNOS 95.57%	60.37%	104.59%	76.97%	77.39%	—
	—	—	—	Difference	35.2%	3.65%	18.6%	18.18%	3.65–35.2
2 ACs	19.67 ± 0.68	45.97 ± 0.61	2,721.30 ± 84.48	NO 94.82%	23.61 ± 1.57	123.92 ± 24.11	—	—	—
	94.82%	134.01%	116.02%	—	87.39%	88.31%	—	—	—
	—	—	—	Difference	7.43%	6.51%	—	—	6.51–7.43
3 ACs	16.29 ± 0.61	30.22 ± 1.84	2,230.70 ± 14.39	eNOS 90.14%	—	—	0.547 ± 0.096	0.717 ± 0.061	—
	78.77%	90.14%	117.62%		—	—	48.98%	98.73%	—
	—	—	—	Difference	—	—	41.16%	8.59%	8.59–41.16
10 ACs	19.24 ± 1.39	29.52 ± 2.66	11,911.43 ± 70.90	NO 97.78%	25.22 ± 2.52	118.52 ± 14.81	0.904 ± 0.095	0.765 ± 0.080	—
	97.78%	88.19%	86.16%	eNOS 88.19%	96.37%	91.43%	153.06%#	114.01%	—
	—	—	—	Difference	1.41%	6.35%	55.28%	16.23%	1.41–16.23

#: As strong prokinetic trait docking traditional therapy; 2 ACs: Saikosaponin A + hesperidin; 3 ACs: Saikosaponin A + hesperidin + tangeretin. V: Vehicle; RAECs: rat aortic endothelial cells; BSS: *Bupleurum chinense* Shugan-San; eNOS: endothelial nitric oxide; GE: gastric emptying; MH: meranzin hydrate; S: Sham; VTI: velocity-time integrals; FA: ferulic acid.

The Ghr-driven SRN

0.083, 1, 12 and 24 h post-AFS rat's peak values synced with peak values of blood biochemicals of three in the immobility (CRH > MDA > IL-6, $P < 0.05–0.001$ vs. S), nine in coronary disorder (ROS > H_2O_2 > TMAO > SOD > MDA > NO > eNOS > ET-1 > MEP-1, $P < 0.05–0.0001$), eight in hypomotility (Ghr > 5-HT > DA > CRH > ACTH > TNF-α > IL-6 > IL-1β, $P < 0.05–0.001$) and three in reduced jejunum stripe tension (BDNF > CORT > NA) (Figure 2). The eight peaks ranked mrni of 0.083 h B-immobility 1.67 > 24 h B_2's 1.17 > 1 h B_1's 0.85 > 24 h ex vivo jejunum tension 0.79 > 1 h C's 0.49 > 24 h G's 0.36 (for refractory root plus butyrate 14.95 as 15.31) > 24 h E's 0.32 > reduced psychopathology 0.28. Of these, (i) the highest immobility peak in 0.083 h post-AFS in rats heterogeneously synced with the increases in human plasma catecholamine post-multiple 6-s sprint interspersed with 30-s recovery [24], whereas lacking catecholamine evidence in the brain decays seconds post-stress [25]. 0.083 → 1 h → 24 h of ↓ butyrate + → +++ via dysbacteriosis is inversely related to immobility, and GE hypomotility – → + (Figure 1); (ii) the 1 and 24 h time points were selected as two inherent cornerstones of multimorbidity because they were associated with nine and three plasma biochemical peaks, syncing these from hippocampus, aorta and G-antrum (Figure 2B). BDNF immunoreactive bands differed across tissues, with a predominant band at ~28–35 kDa in aorta and ~14–15 kDa in gastric antrum. These signals were therefore quantified as the major tissue-specific BDNF-immunoreactive bands, partly similar to these past findings [6, 9]. This tissue-specific observation was interpreted within the B_1CB_2GE multimorbidity framework, whose depression-cardiovascular component is consistent with epidemiological evidence linking emotional triggers, depression, myocardial infarction, coronary heart disease, and broader multimorbidity [26–28].

Through five functional ACs, the Shugan-like therapy captured both the dynamic features and quantification of post-AFS 1–24 h B_1C-B_2GE five-disease cluster dimensions, along with associated plasma biochemical molecule levels in the rat Gan axis, representing the dual or multidirectional post-AFS interactions of BCGE [29] (Figure 1). This serves as a paradigm for a multimorbidity modeling mechanism framework, uniquely positioned among 549 publications (9 involving three-disease models and 540 involving two-disease models). The elaborately tailored, BSS-derived multifunctional AC tools and their corresponding multi-disease targets function like a tenon-and-mortise mechanism—repeatable and precise—akin to how two ACs derived from the phytomedicine *Fructus aurantii* unlock antidepressant and prokinetic functions through modulation of 5-HT_3 and Ghr.

Ex vivo-to-in vivo extrapolation of multifunctional ACs as BSS/BPSDS proxies

We used the established three-step ex vivo-to-in vivo extrapolation framework for AC(s) as BSS proxies of BCGE multifunctions, including vasodilation, entero-gastro prokinetic and antidepressant activities (Figure 3A–C). Across the multi-cell models, the selected AC(s) showed highly comparable CRs to BPSDS/BSS in ex vivo and AFS rats in vivo, with 1st/3rd-vs.-2nd step differences all kept within a low range (Figure 3D), indicating that the inserted rapid ECs step could stably represent the multifunctional contribution profiles of multicellular systems and shared AFS rats (Figure 3A–D).

BPSDS eliminated ex vivo interferences and served as an interference-free herbal proxy

To further optimize herbal ex vivo proxies, we compared direct BSS addition, post-dose serum, and deproteinized BPSDS in the same multicells/ECs-AFS rat framework (Figure 4A–L). Direct addition of BSS caused aortic inactivation and increased EC apoptosis (Figure 4E and F), whereas serum addition still caused organ-bath foam (Figure 4G and H). In contrast, 100°C water-bath deproteinization for 5 min generated BPSDS that preserved multifunction while removing interference from crude preparation, as shown by the absence of aortic inactivation, EC apoptosis, and bath foam (Figure 4D, Figure 4I–K). Quantitatively, BPSDS reduced the interference-associated readouts of inactivation, foam, ROS, apoptosis, IL-6, and TNF-α by 36.64–47.45% (Figure 4L).

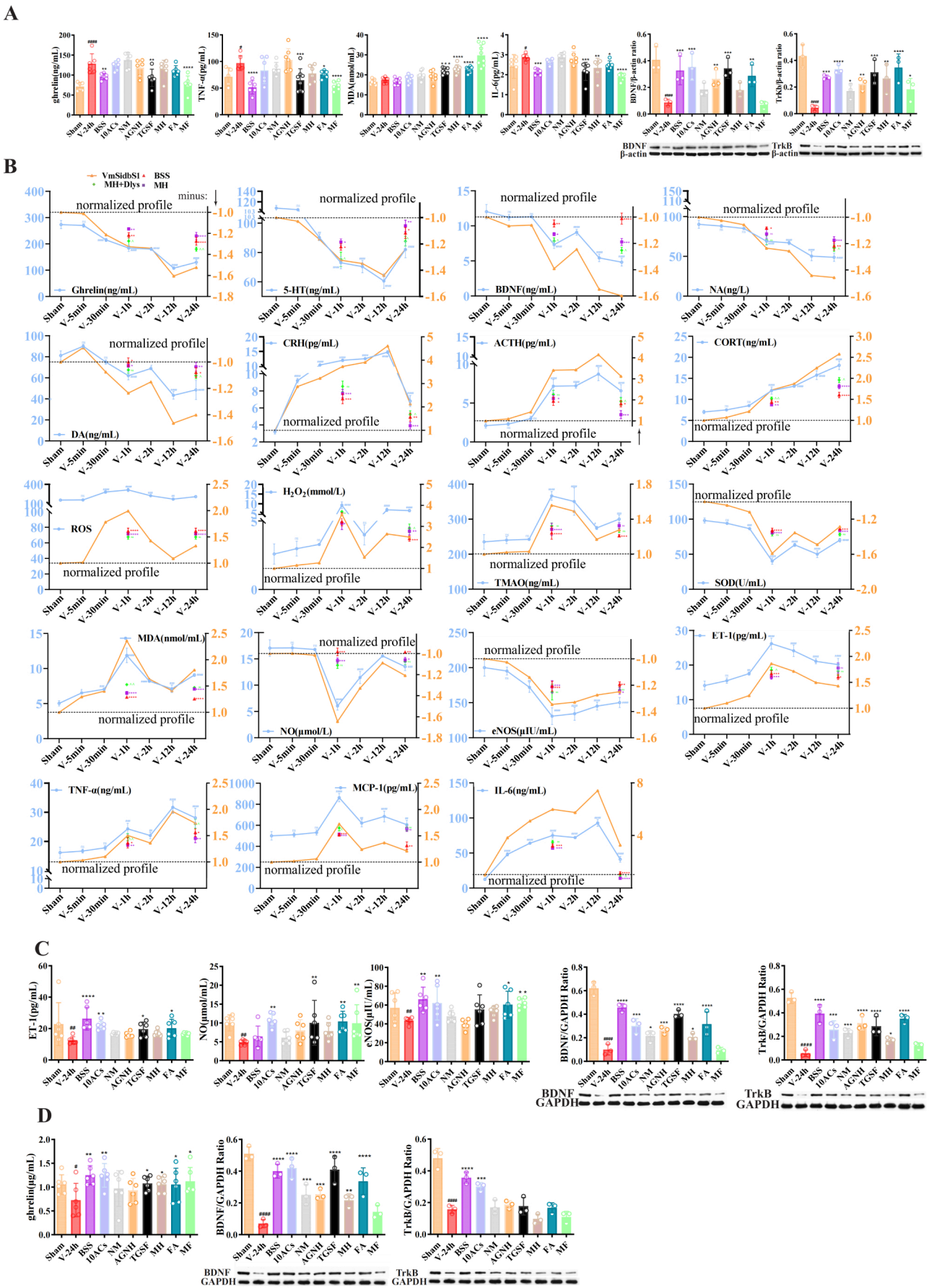

Figure 2. The synchronized profiles of all and part 20 plasma biochemical molecular levels [2 sets of values, plasma molecules (raw data and rni), one set/other organ]. (**A**) Ghrelin (Ghr), BDNF, TrkB, IL-6, TNF-α and MDA in hippocampus; (**B**) Ghr, 5-HT, BDNF, NA, DA, CRH, ACTH, CORT, ROS, H_2O_2, TMAO, SOD, MDA, NO, eNOS, ET-1, TNF-α, MCP-1, and IL-6 in plasma; (**C**) NO, BDNF immunoreactive band at ~28–35 kDa (putative proBDNF), TrkB, ET-1, and eNOS in aorta; (**D**) Ghr,

BDNF immunoreactive band at ~14–15 kDa (putative mature BDNF), and TrkB in gastric antrum. # $p < 0.05$, ## $p < 0.01$, ### $p < 0.001$, #### $p < 0.0001$ vs. Sham; * $p < 0.05$, ** $p < 0.01$, *** $p < 0.001$, **** $p < 0.0001$ vs. V-24 h. V: Vehicle; 5-HT: 5-hydroxytryptamine; BDNF: brain-derived neurotrophic factor; eNOS: endothelial nitric oxide; ET-1: endothelin-1; IL-6: interleukin-6; MCP-1: monocyte chemoattractant protein-1.

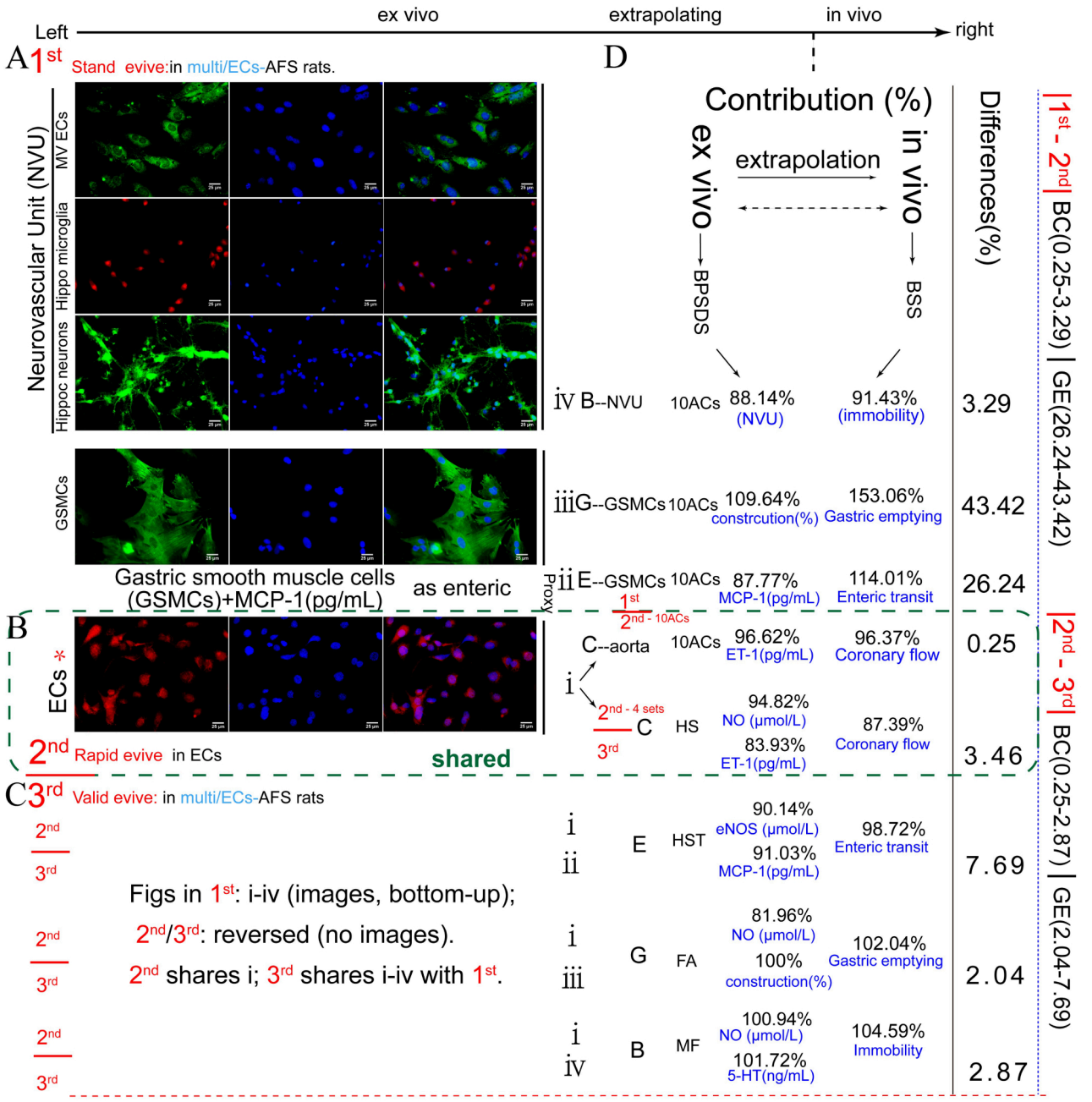

Figure 3. The paragraph of ex vivo to in vivo extrapolation of AC(s) as BSS proxies for vasodilation/entero-gastro prokinetic/antidepressant [CEGB (Coronary-Entero-Gastro-brain) multi-function] in 1st multicells (standard), 2nd ECs (rapid evive), and 3rd multicells (validation). The workflow proceeds from left to right, showing ex vivo-to-in vivo extrapolation. In the top left part of Figure 3 is the image of the Cell Painting assay protocol of neurovascular unit (microvascular ECs, hippocampal microglia, hippocampal neurons), Ach-treated gastric smooth muscle cells, and ECs. In the right part of the image is the comparison of the contributions of ex vivo and in vivo administration. Up to down of (**A**) 1st standard evive → (**B**) 2nd rapid evive → (**C**) 3rd validation of evive, including each disease's contribution, accuracy range, and differences between those 3 steps. (**D**) The contribution comparisons of ex/in vivo extrapolation (evive) of ACs as BPSDS/BSS proxies for multifunctions in 1st standard or 3rd validated multicells + AFS rats vs. 2nd ECs + AFS rats, i.e., 1st, 2nd and 3rd systems each and contribution comparison of 1st/3rd vs. 2nd. The differences are obtained by subtracting each step minused and taking the absolute value. 4 sets of AC(s) were used in both 2nd and 3rd step multifuntional ACs. HS: Saikosaponin A + hesperidin; HST: HS + tangeretin; FA: ferulic acid; MF: MH + FA; Hippo: hippocampal; MV: microvascular; ECs: endothelial cells; Ach: acetylcholine; AFS: acute forced swimming; BSS: *Bupleurum chinense* Shugan-San; MH: meranzin hydrate.

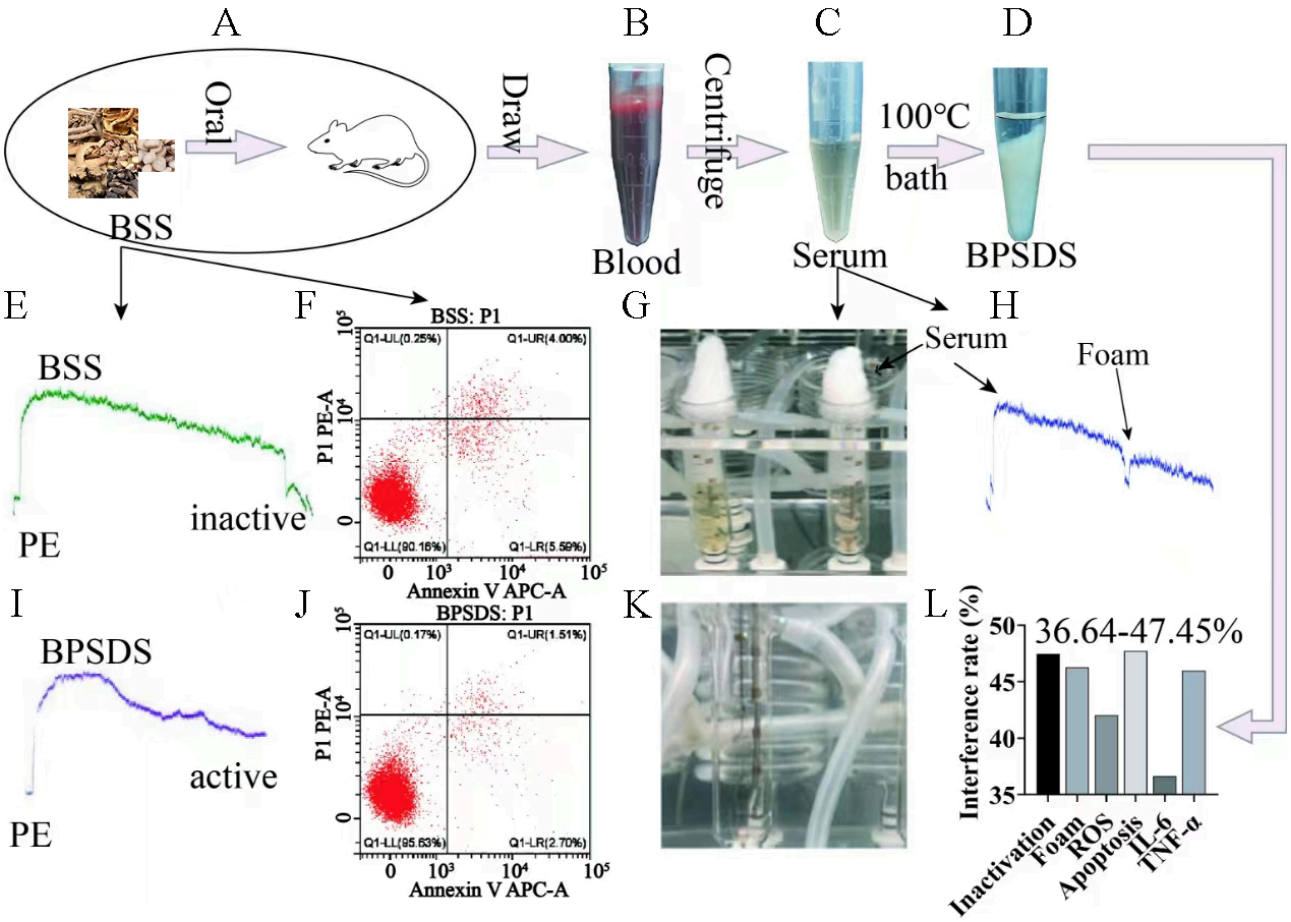

Figure 4. Graphic comparison of ex vivo-to-in vivo extrapolation of ACs as multifunctional contributors to BPSDS/BSS in multicells/ECs-AFS rat. (**A**) Left BSS of directly addition into ex vivo system as the first popular ex vivo herbal agent method; (**B**, **C**) post-dose herb extract of serum as the proxy of herbal ex vivo agents of purported interference-free when added into ex vivo system; (**D**, **I**) 100°C water bath for 5 min to obtain BPSDS (BSS postdose supernatant of deproteinized serum) without interferences of aortic inactivation, EC apoptosis (**J**) and foam in organ bath (**K**), while adding BSS caused aortic inactivation (**E**), ↑ EC apoptosis (**F**) and adding serum caused ↑ foam (**G**, **H**); (**L**) quantitative interference eliminated by BPSDS was evaluated by change percentage of inactivation, foam, ROS, apoptosis, IL-6, TNF-α (36.64–47.45%). AFS: acute forced swimming; BSS: *Bupleurum chinense* Shugan-San; ECs: endothelial cells; IL-6: interleukin-6.

Three new normalization algorithms corrected the bias of orthodox model, drug, and phytochemical evaluation methods

We next compared three pairs of distinct new-old algorithms. Methodologically, mrni, drni, and prni served different purposes: mrni normalized model deviation across different endpoints, drni quantified drug-induced correction relative to the model background, and prni estimated phytochemical contribution after subtracting the S-V bias. Together, these indices reduced raw-value distortion and improved cross-endpoint comparability in the present study, namely mrni as new formula 1, drni as new formula 2, and prni as new formula 3, vs. the orthodox or popular calculations that separately handled S and V or directly compared ACs with herbs (Figure 5A–J). These new formulae were used to eliminate calculation-related biases.

Ghr/Src-PI3K/Akt-eNOS signaling

As a representative vasoactive AC, FA induced dose/E+ vasodilation in aortic rings, which can be abolished by D-Lys, ODQ, LY294002, PP2 and L-NA, indicating positive involvement of Ghr (Figure 6A). In H-ECs, H_2O_2 increased ROS and reduced NO, both reversed by FA; the inhibitory effect of these FA-induced reversions was mainly caused by D-Lys (Figure 6B). Western blot showed that Ghr, p-Src, p-PI3K, p-Akt and p-eNOS were decreased in H-ECs vs. S and can be restored by FA, while these restored proteins were again abolished by D-Lys, PP2, LY294002, ODQ and L-NA (Figure 6C). Under oxidoreductase intervention, the FA-restored phosphorylated proteins ranked as PEG-catalase > PEG-SOD > MnTMPyP, showing NO-bioavailability activation's anti-oxidative sensitivity (Figure 6D).

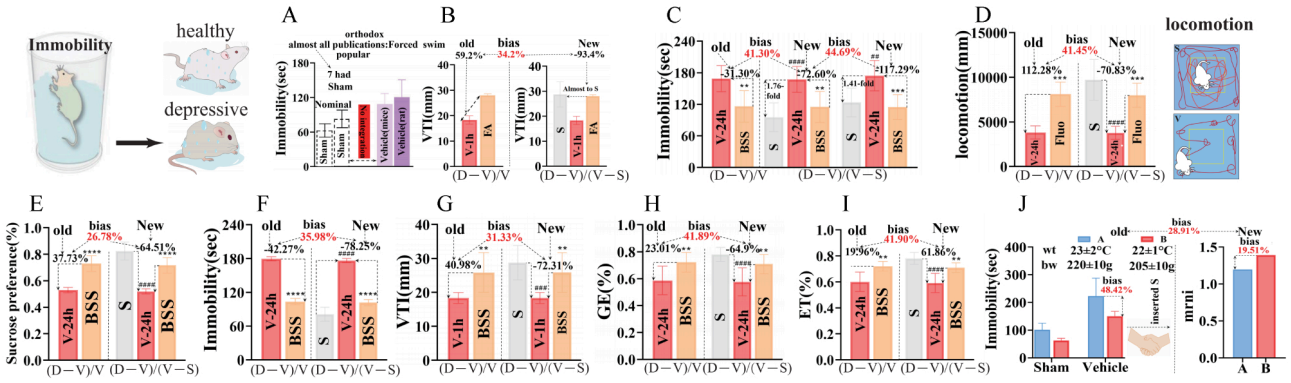

Figure 5. The difference comparison of three pairs of distinct new old algorithms. Model raw normalization increment (mrni) as new formula 1 vs. old or popular V; drugs responses of (Drug – V)/(V – S) as new formula 2 (drni) vs. old or popular [(Drug – V)/V], and phytochemical action contribution of [(ACs – V) – (V – S)]/[(BSS – V) – (V – S)] as new formula 3 (prni) vs. ACs/herbs. (**A**–**J**) S and V are not calculated by formula 1 and only S was used as subject of comparison and orthodox statistics following compared with V, without two-in-one as new value, without showing true relationship and resultant modeling value bias; 59.2% was FA vasodilator strength from old formula (Drug – V)/V, FA's 93.4% from new formula 2, resultant their bias was 34.2% whose 28.75 mm (VTI, E+ CFMD or coronary flow) was absent as S. $^{\#}$ $p < 0.05$, $^{\#\#}$ $p < 0.01$, $^{\#\#\#}$ $p < 0.001$, $^{\#\#\#\#}$ $p < 0.0001$ vs. S; * $p < 0.05$, ** $p < 0.01$, *** $p < 0.001$, **** $p < 0.0001$ vs. V. V: Vehicle; S: Sham; BSS: *Bupleurum chinense* Shugan-San; FA: ferulic acid.

D-Lys identified Ghr as the shared pluripotent abolisher of multifunctional AC anchoring

Among several inhibitors tested against MH- or different sets of ACs-induced multifunction pharmacodynamics, the Ghr antagonist D-Lys showed the broadest and strongest abolishing effect in vivo across four BCGE-like functions (Figure 7A). Accordingly, D-Lys abolished 17.17–39.09% of the BCGE-4 functions induced by the strongest 3 sets of 2–3 AC(s), with rankings relatively similar to ex vivo results. In H-EC-based mimic ex vivo systems, D-Lys also abolished cross BCGE-like, ROS, and NO readouts, ranking top 1 in six units, including 3 NO and 2 ROS indices (Figure 7B and C). After in vivo pretreatment, D-Lys mainly abolished MH-contributed BGE 3-functions (Figure 7D).

Time-dependent dendritic psychopathology after AFS and its reversal by Shugan-like therapy

AFS induced time-dependent dendritic psychopathology in dentate gyrus (DG) neurons, as shown by representative apical dendritic segments (Figure 8A) and quantitative analysis (Figure 8B). Total dendritic spine density was reduced at 12 and 24 h post-AFS, whereas total dendritic length mainly decreased at 12 h; in contrast, the number of intersections remained unchanged (Figure 8B). After intervention, BSS, MH, and FLX all improved the AFS-induced reductions in dendritic spine density and dendritic length (Figure 8C), together with restoration of GluA1, postsynaptic density protein 95 (PSD95), and BDNF in the DG (Figure 8D). HE staining of the heart and transmission electron microscopy of hippocampal synapses further showed that Shugan-like therapy alleviated structural injury in both myocardium and hippocampal synaptic ultrastructure after AFS (Figure 8E).

Discussion

The reasons for selecting 1 h B_1C and 24 h B_2GE as five indivisible and structurally stable mono-disease targets are their consistent and repeatable presence post-AFS. Additionally, selecting 24-h depression ($Brain_2$), based on two immobility time responses to drug administration, as a holistic representative of the functions, allows convenient comparative observation [3, 6–11, 16, 17, 30–34] while avoiding exponential complexity from multimorbidity. Among 0.083, 0.5, 1, 2, 12, and 24 h post-AFS (Figure 1), selectively representative positive time-points of the MH series-induced multifunction, especially the immobility time peak value in rats with B_1CB_2GE phenotypes, are the 3rd and 6th, but not the 1st. The peak values of 17 indices of excitatory neurotransmitter, HPA hormone, oxidative molecular, inflammation, endothelial system, gut bacteria metabolite, MDA, and Ghr are consistent with those from primary immobility time at post-AFS 1 h but not 0.083 h (Figures 1 and 2). These post-AFS temporal depressive-like behavior dynamics have not been reported before in any review of depressive animal modeling [30–34].

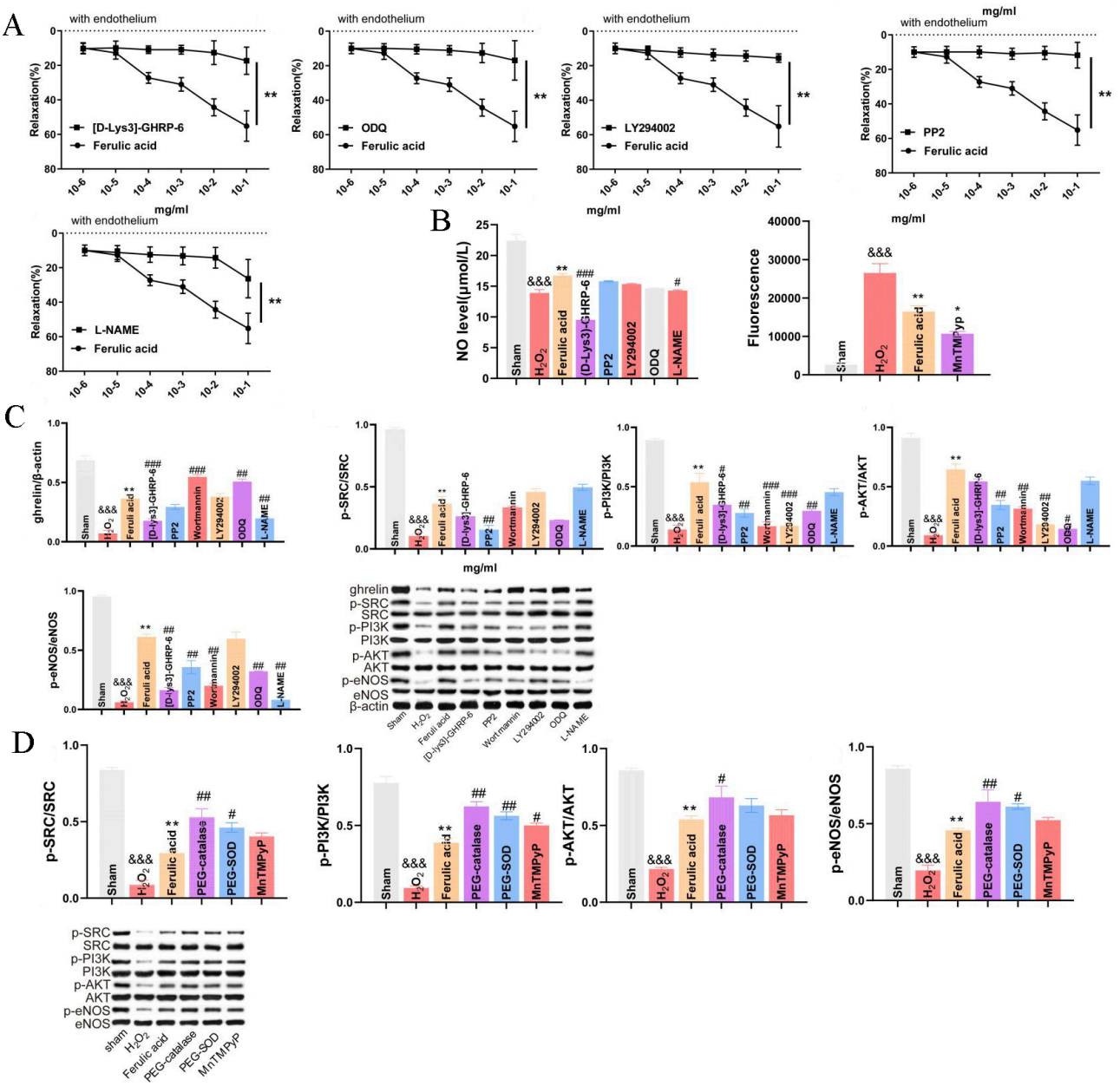

Figure 6. The endothelium-dependent (E+) vasodilation induced by escalating dose FA in isolated aortic rings and H_2O_2 -treated endothelial cells (H-ECs) via a parallel dual upstream ghrelin (Ghr)/Src-PI3K/Akt-eNOS, an anti-oxidative sensitivity, and subsequently activating the bioavailability of nitric oxide (NO) signaling pathway. This pathway was examined using six inhibitors [Ghr receptor's D-Lys 25 μmol/L, Src kinase's PP2 10 μmol/L, Akt's wortmannin 0.1 μmol/L, PI3-kinase LY294002 30 μmol/L, endothelial NO synthase L-NAME 100 μmol/L, soluble guanylyl cyclase (ODQ) 1 μmol/L] and three artificial oxidoreductases, i.e., poly-ethyleneglycol-superoxide dismutase (SOD) (PEG-SOD) as the membrane permeant analogue of catalase (PEG-catalase) 500 μmol/L, PEG-SOD 100 units/mL and cell-permeable SOD mimetic (MnTMPyP) 100 μmol/L. (**A**) E+ vasodilation induced by escalating dose of FA in endothelium-intact isolated aortic rings and was abolished when pretreatment of D-Lys, ODQ, LY294002, PP2, and L-NA, respectively, identifying positive regulation of Ghr, Src, PI3K, Akt, and eNOS. (**B**) NO was detected by the NO kit. The generation of ROS in H-ECs was increased by 200 ng/mL FA. 0.5 mmol/L hydrogen peroxide-loaded ECs were stimulated with FA, and the ethidium bromide fluorescence was monitored over 10 min using a confocal microscope. H_2O_2 reduced levels of NO via impaired endothelium in ECs, and reversed by FA, while these reversions were markedly abolished when pretreatment of D-Lys, PP2, LY294002, ODQ, and L-NA for NO level and of MnTMPyP for ROS level in H-ECs. (**C**) Western blot analyses showed that the levels of Ghr, p-Src, p-PI3K, p-Akt, and p-eNOS were ↓ in H-ECs compared with S and reversed by FA. The latter ↑ levels of Ghr, p-Src, p-PI3K, p-Akt and p-eNOS were all markedly abolished by pretreatment of D-Lys, PP2, LY294002, ODQ and L-NA. D-Lys (Ghr) and PP2 (Src) without interaction, abolished middle/downstream inhibitors of roles and not abolished by them except for D-Lys with stronger mutual abolitions with L-NA, embodying a parallel dual upstream of Ghr/Src-PI3K/Akt-eNOS pathway as a regulation mechanism of FA-rising vasodilation. (**D**) Modeling, FA dose, or the changes in the levels of Ghr and phosphorylated pathway protein are the same or nearly the same as those in part (**C**). V's p-Src, p-PI3K, p-Akt, and p-eNOS levels were lower than S, while FA's these were higher than V. We compared FA-rose phosphorylated pathway protein levels in the presence and absence of three artificial oxidoreductases, such as ROS, etc., evidencing damaging E+ vasodilator pharmacology, resultant ranking when present were PEG-catalase (↑ p-Src/PI3K/Akt/eNOS levels) > PEG-SOD (↑ p-Src/PI3K/eNOS levels) > MnTMPyP (↑ p-PI3K level), as direct evidence of anti-oxidative sensitivity of activating bioavailability of NO pathway. $^{\&}$ $p < 0.05$, $^{\&\&}$ $p < 0.01$, $^{\&\&\&}$ $p < 0.001$, $^{\&\&\&\&}$ $p < 0.0001$ vs. S; * $p < 0.05$, ** $p < 0.01$, *** $p < 0.001$, **** $p < 0.0001$ vs. H_2O_2. $^{\#}$ $p < 0.05$, $^{\#\#}$ $p < 0.01$, $^{\#\#\#}$ $p < 0.001$, $^{\#\#\#\#}$ $p < 0.0001$ vs. FA. ECs: endothelial cells; eNOS: endothelial nitric oxide; S: Sham; FA: ferulic acid.

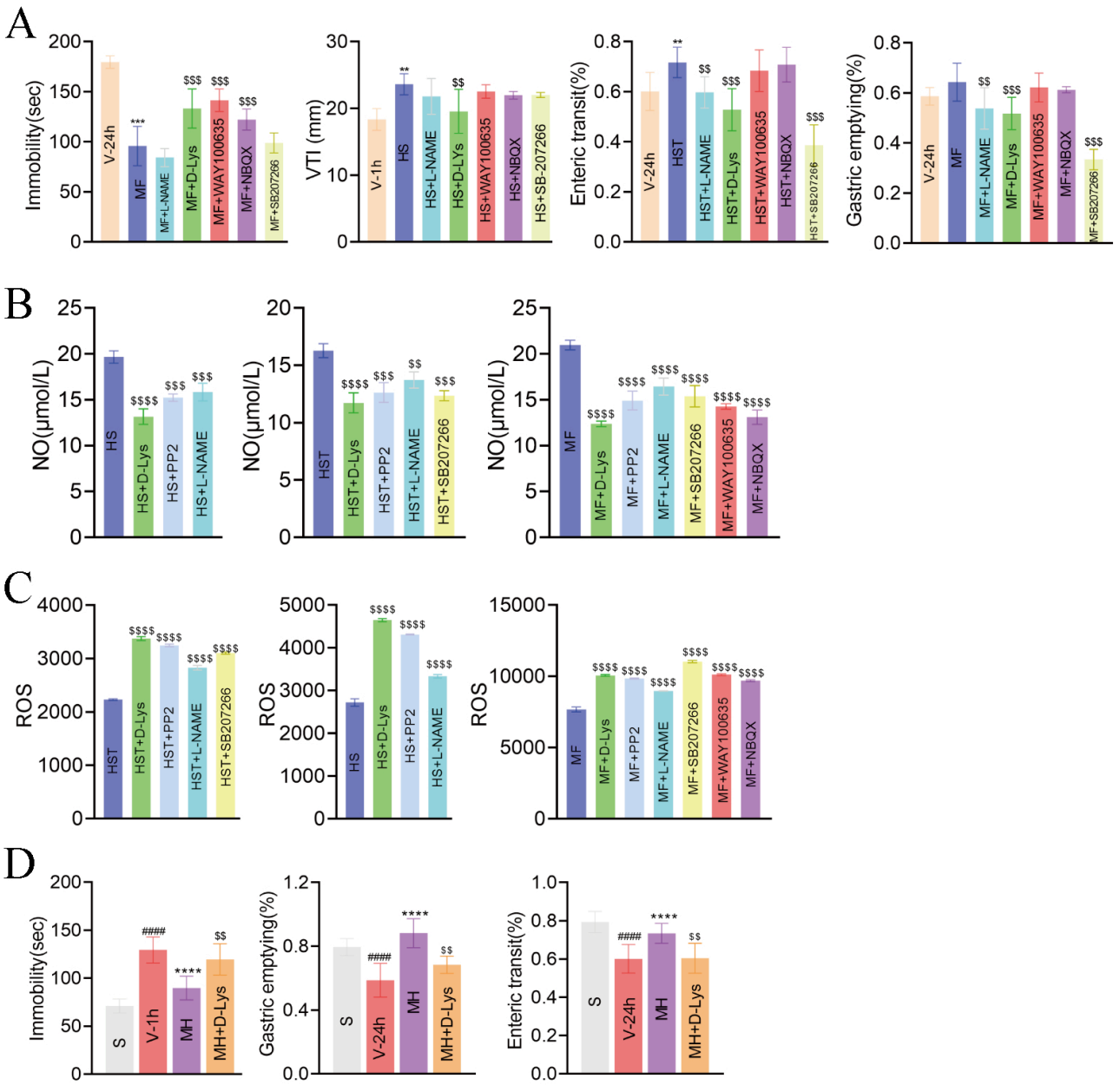

Figure 7. Multifunction comparisons between several doses of ontological disease pathogenesis or function inhibitors using pretreatment of abolishing prokinetic-based pluripotent MH or 4 sets of multi-ACs induced multifunction pharmacodynamic in vivo and mimic ex vivo. (**A**) Ghrelin (Ghr) inhibitor D-Lys: abolishing 4 sets of 2–3 ACs-induced C (inhibitors D-Lys, L-NA) BGE (plus WAY100635, NBQX and SB207266) multifunctions in vivo: among above ontological in vivo bioactivity of 5 pairs inhibitors and 4 functions (BCGE-like ↑ immobility, ↑ coronary disorder, ↓ G-emptying, ↓ enteric transit), D-Lys is pluripotent (4 rather than 1 functions were effective) and the strongest (three were top 1, one as top 2 inserted the middle of 2 depressive inhibitors) while other 4 inhibitors (2 shared depression inhibitors, one vasoactive, one hypomotility) only half of depressive inhibitor was top 1. (**B**) The inhibition rate to in vivo BCGE multifunction-induced by the strongest 3 sets of 2–3 ACs when pretreatment of Ghr antagonist D-Lys, which abolished ACs-contributed 17.17–39.09% BCGE-4 function as top 1 (brain-coronary-gut of three disorder of: one item D-Lys top 1 and two top 2 > other 4 inhibitors ranking), relatively similar to their ex vivo conclusion. (**C**) D-Lys, when pretreated, abolished 4 sets of 2–3 ACs-induced mimic ex vivo index strength of multifunction of BCGE (inhibitors of: C = D-Lys, L-NA and PP2; E = C + SB207266; parallel B and G = E+ WAY100635 and NBQX, above sum × 2 = ROS and NO of parallel 38 indices in H-ECs), as BCGE-like (depressive 2 inhibitors, one prokinetic inhibitor with GE-hypomotility and vasodilator L-NAME), antioxidant and pluripotent Ghr inhibitor of 6 function ex vivo model. And thereinto D-Lys was a shared protagonist (its 6 units, including 3 NO and 2 ROS indices as top 1). (**D**) The pretreatment of D-Lys mainly abolished MH-contributed in vivo BGE 3-functions whose another increase in E+ CFMD was invalid, which was replaced by effective ferulic acid or HS in Table 2. $^{\$}$ $p < 0.05$, $^{\$\$}$ $p < 0.01$, $^{\$\$\$}$ $p < 0.001$, $^{\$\$\$\$}$ $p < 0.0001$ vs. MH or HS or HST or HS; * $p < 0.05$, ** $p < 0.01$, *** $p < 0.001$, **** $p < 0.0001$ vs. V-1 h or V-24 h. $^{\#}$ $p < 0.05$, $^{\#\#}$ $p < 0.01$, $^{\#\#\#}$ $p < 0.001$, $^{\#\#\#\#}$ $p < 0.0001$ vs. Sham (S). CFMD: coronary flow-mediated dilation; GE: gastric emptying; MH: meranzin hydrate.

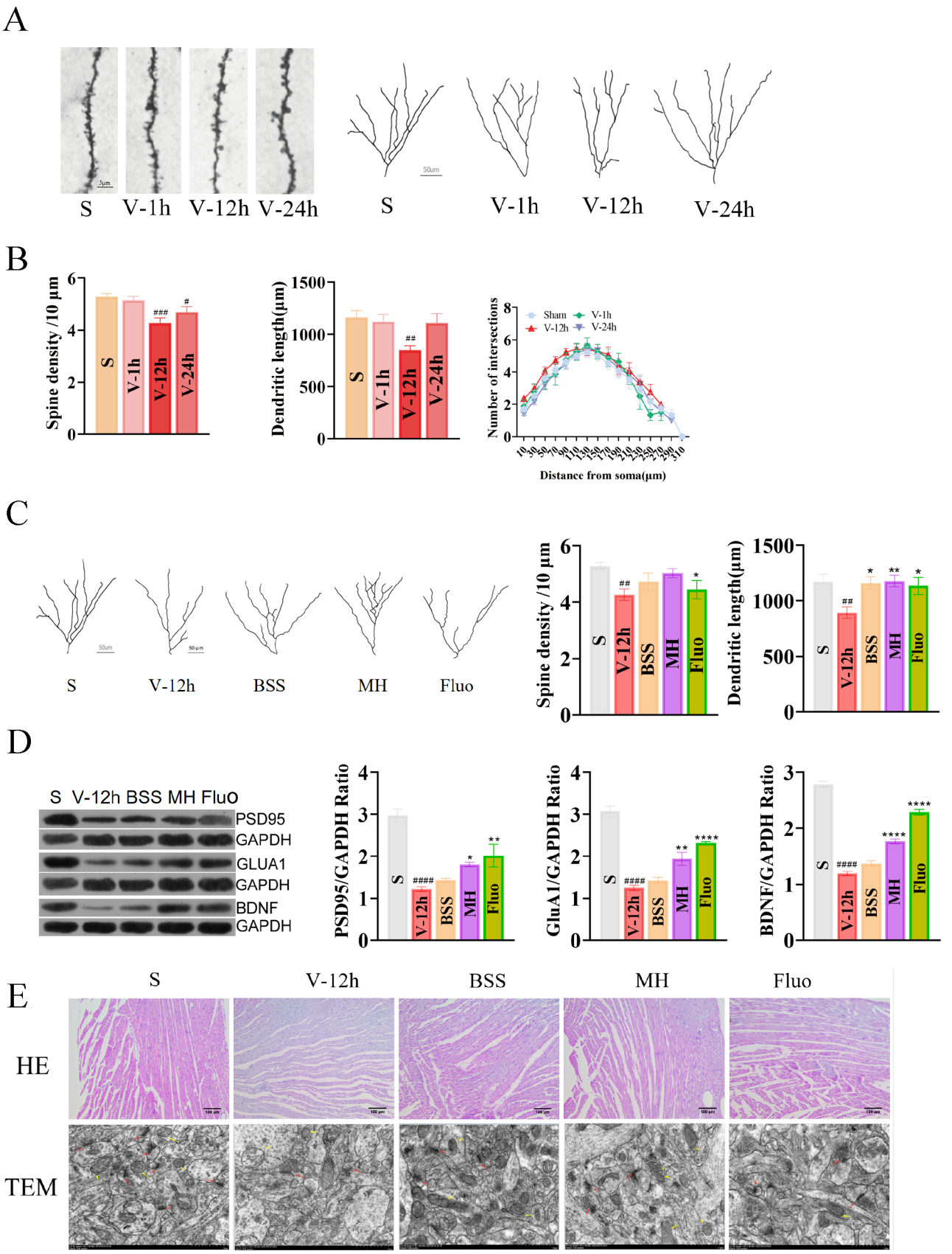

Figure 8. Changes of total dendritic spine density and dendritic length after time-dependent acute forced swimming (AFS). (**A**) Representative examples of apical dendritic segments of DG pyramidal neurons selected for quantitative analysis of dendritic spines from the different experimental groups of animals. Scale bar represents 50 μm. (**B**) Total dendritic spine density. (**C**) Effect of BSS (30 g/kg), MH (6.81 mg/kg), and Fluo (10 mg/kg) on changes induced by AFS on total dendritic spine density, dendritic length and expression of PSD95, GluA1 and BDNF protein in DG. Representative examples of apical dendritic segments of DG pyramidal neurons selected for quantitative analysis of dendritic spines from the different experimental groups of animals. Scale bar represents 50 μm. Total dendritic spine density. Total dendritic length. (**D**) Western blot: expression of

phospho-AMPA receptor 1 (GluA1), PSD95 and BDNF protein. The expression of GluA1, PSD95 and BDNF was quantified using Image Pro Plus software. (**E**) S group and effect of BSS (30 g/kg), MH (6.81 mg/kg) and Fluo (10 mg/kg) on changes induced by AFS. HE-staining of heart, Bar = 100 μm. Representative transmission electron microscopy images revealing the ultrastructure of synapses in the hippocampus (12,000×, scale: 1,000 nm). * $p < 0.05$, ** $p < 0.01$, *** $p < 0.001$, **** $p < 0.0001$ vs. BSS. # $p < 0.05$, ## $p < 0.01$, ### $p < 0.001$, #### $p < 0.0001$ vs. S. One-way ANOVAs followed by *Q* tests were used. Data are expressed as the mean ± S.E.M of the number of dendritic spines/10 μm of dendritic segment (n = 4–5 animals, 15–25 dendritic segments, 600–1,400 μm total length). BDNF: brain-derived neurotrophic factor; BSS: *Bupleurum chinense* Shugan-San; DG: dentate gyrus; MH: meranzin hydrate; PSD95: postsynaptic density protein 95; S: Sham.

The conventional post-AFS 24-h single-disease depressed rat brain model has been redefined as a five-disease cluster consisting of temporal trajectories of 1-h medium depression ($Brain_1$) and cardiac event (Coronary), 24-h heavy depression ($Brain_2$), and gastroenteric hypomotility (GE), differing from the previously fixed 24-h B_2GE-like model of heavy depression and GE-hypomotility [3, 6–11, 16, 17] (Figure 1). Ex vivo mimetic indices for B_1CB_2GE were derived from single-cell models, such as H-ECs [5], and multicellular models, including corticosterone-treated NVUs composed of HN, microglia, and microvascular ECs, representing the cellular communication system involved in neurovascular coupling and depression-related cerebral blood flow [35]. Additionally, Ach-treated gastric smooth muscle cells (A-GSMCs) [36], responsible for GE, along with H-ECs [5], served as ontological and proxy models for the B_1CB_2GE five-disease cluster (Figure 3). Above multifunctional CR differences ex/in vivo of selected ACs (first 10 ACs, then 10 ACs and MH) to BPSDS/BSS were respectively compared or validated with the same CR differences in a half-year interval (Table 1), and two times in multicellular models (one as a standard of BAPevive and another as a validation). Two multicellular models, each incorporating single-cell H-ECs as intermediate proxies, were used alongside AFS and MH-series conditions. Upon administration of BPSDS, BSS, and their associated ACs, several SRNs were detected, demonstrating that this multifunctional tool effectively anchored multiple phenotypes through SRNs (Figure 4), particularly involving the shared driver, Ghr. We used two sets of multicellular models—the first and third as criteria and validation, with the second H-EC model inserted to apply BAPevive. The resulting contribution differences between 10 ACs and 10 ACs + MH to BPSDS and BSS were < 4.23% (Figure 3). Yet, ontological H-ECs completely represent the changes in multiorgan-derived cellular pathophysiology, supporting multifunctional BAPevive.

Following innovative idea, optimized method, and normalization calculation described later, the BAPevive-based CR and minimal ex/in vivo differences of AC-induced functions to BSS/BPSDS-BSS were 96.37–103.8% and 1.41–18.60 among BCGE ranges (60.37–153.06%/1.41–69.31%) from five sets of AC(s)-induced same indices, their contribution difference to BSS is only 3.63–3.8%, suggesting almost 100% bioequivalence—a result not previously reported for herbal multifunctional phytochemicals contributions, similar to ~6% difference rates of mono-functional CFMD by syringic acid and FA to grape/its PSDS [5], different from our previously reported 2–5 herbal mono-/3-functional contributing ACs alone [3, 6–11, 16, 17]. With our optimized CR calculation formula (Figure 5), among 10 ACs as early contributors to BSS-induced four function, the contribution orders from five sets of AC(s), plus BSS called MH series, to herbal BSS/BPSDS are (%) B's MH + FA 104.59 > MH 103.84 > 10 ACs 91.43 > FA 90.36 > HS 88.31 (max vs. min difference 17.01), C's (%) FA 112.28 > 10 ACs 96.37 > HS 87.39 > MH 73.94 > MH + FA 60.37 (difference 51.01), G's (%) 10 ACs 153.06 > MH 146.65 > FA 102.04 > MH + FA 76.97 > HST 48.98 (difference 104.08), and E's (%) FA 151.27 > 10 ACs 114.01 > MH 104.14 > HST 98.73 > MH + FA 77.39 (difference 73.88) (Figure 3) (Table 1). Interestingly, each of the manifestation profiles of four functions of five sets of AC(s) pre- and post-administration to subjects is (i) first reported 30.4–43.6% independent multifunction without interaction, as a herbal pharmacology in which although predefined contents range of some index phytochemical(s) were low, parent herbal efficacies are legitimately explained from "unexpectedly" and presently existing non-predefined effective phytochemical(s) observed, which is only previously missed, and not reported before, and (ii) 54.5–25.4% synergistic or antagonistic with the increase or decreases in pharmacodynamic responses, similar to those in Chinese medicinal formula Realgar-Indigo naturalist [37], grape, GXII and ZHIQIAO-HOUPU decoction [1, 3, 5].

Overall, 3–4 functions of the BGE- and BCGE-like 10 ACs have been reported in homogeneous comparisons with the parent herbal BSS [4]. However, each of the 10 ACs, based on accumulated evidence, demonstrated responses to distinct single-disease models, thereby heterogeneously covering BCGE-like multifunctionality without consistent or homogeneous supporting evidence.

Remarkably, each component of the Shugan-like MH series (BSS and five sets of four functional ACs), tailored over the past 14 years, has closely replicated the combined efficacy of SSRIs, isosorbide, and MOS—targeting antidepressant effects (↑ immobility), vasodilator (↑ E+ CF), and prokinetic actions (↑ gastric emptying, ↓ IT) [3, 6–11, 16, 17]—which previously aggravated multimorbidity when treated within a single-disease framework [18–22]. Interestingly, from 2011 to the present, we have chronologically anchored 10 instances of three-disease clusters (24-h post-stress BGE) within a single AFS model—termed the "depressed rat" [3, 6–11, 16, 17]—rather than using multiple independent models for depression, gastrointestinal, and coronary disorders, as originally proposed in the separate modeling protocol.

To investigate the shared Ghr-driven mechanism underlying MH-induced multifunctional effects, we employed single-cellular H-ECs in combination with AFS rats as precise proxies for B_1CB_2GE-like multicellular and multimorbidity models (Figures 1 and 3). ECs form the foundation of functional organ systems [38] and mediate blood oxygen level-dependent neurovascular coupling [35]. NO synthase interacting protein (NOSIP) plays a key role in regulating GE hypomotility [39]. Accordingly, H-ECs were designed to detect the inhibitory effects of the strongest MH-induced multifunction and underlying mechanisms through pretreatment with consistent doses of various inhibitors, including the gastro-derived Ghr antagonist D-Lys, eNOS inhibitor (L-NA), Src kinase inhibitor (PP2), TNF-α receptor blocker (1R-7050), AMPA receptor antagonist (NBQX), chronic antidepressant pathway blocker (FLX-WAY100635), and the 5-HT4 receptor antagonist (SB207266) used in the prokinetic pathway (Figure 6).

Using the strongest multifunctional and prokinetic MH compounds—supported by pluripotency-based activity and three normalization calculation formulae—Ghr was found to drive SRNs that regulate post-AFS temporal B_1C-B_2GE five-disease clustering across systems, geographic regions, time-space scales, clinical specializations, and both traditional and modern therapies, surpassing conventional heterogeneity limited to organ, sample, or specialty [40–42] (Figure 1) (electromyography and gait data) [43].

Using 20 plasma (Figure 2B) biochemical molecules relevant to temporal B_1C-B_2GE lock cylinders groove components easily inserting multifunction ACs key bulge, the former 12 as lock cylinders installed inside lock body of primary B_1 and secondary B_2GE, i.e., Ghr-driven acute stress system-inflammatory-BDNF's psychopathology [27, 28, 44–47] as cylinder mechanism, the latter 8 as cylinders docked 1 h ↓ E+ CFMD lock body. TMAO (trimethylamine *N*-oxide) acts as an upstream of IL-6 impairment, reducing endothelial NO [48, 49] and butyrate levels for ↑ immobility via methylated-DNA regions and ↓ hypomotility [50, 51] (Figures 1, 2, and 7).

The defining driver traits of Ghr were demonstrated as follows: (i) D-Lys in H-ECs ranked first in overall strength and breadth of inhibition against MH-induced multifunction among eight inhibitors, including the eNOS inhibitor L-NA. (ii) D-Lys also reversed the MH-induced reduction in the number and length of apical dendrites in DG-derived neurons in AFS rats with the B_1C-B_2GE multi-phenotype. This distinct change is caused by AFS alone, which altered dendritic morphology only in newborn granule neurons [52]. Such acute psychopathology, which was abolished by Shugan-like MH, may represent an early trajectory toward chronic depression and has long been overlooked [53], which may also change multimorbidity research. The above psychopathology of the dendritic morphology (Figure 8) is the marker of not only multimorbidity between primary and secondary, but also organic depression. (iii) Most importantly, AFS rats were used to validate the shared Ghr-driven SRNs mediating multimorbidity clusters. Among the nine tested inhibitors, D-Lys emerged as the most potent and comprehensive in counteracting MH-induced multifunction, anchoring the B_1C-B_2GE five-disease cluster. Previous Shugan-related studies have provided heterogeneous evidence for antidepressant, gastroenteric prokinetic, vascular, inflammatory, oxidative, and Ghr-related regulatory effects in post-AFS or related disease models [3, 6, 9–11, 16, 17, 54]. However, these studies mainly examined single phenotypes, limited brain-gut clusters, or

heterogeneous disease settings, rather than a unified temporal multimorbidity trajectory. In contrast, the present study provides homogeneous evidence within the same AFS-induced B_1CB_2GE trajectory model, showing that D-Lys consistently abolished MH/ACs-induced multifunctional anchoring effects, thereby identifying Ghr signaling as a shared driver of the five-disease multimorbidity trajectory. To our knowledge, no previous publication has reported fixed or temporal complex multimorbidity cluster modeling with non-random, post-stress-induced shared risk factors as presented here.

An updated methodology using the AFS rat model incorporates temporal 1-h B_1C to 24-h B_2GE five-disease trajectories, divided into upstream molecular regulation, midstream circulatory biochemical changes, and downstream five-disease phenotype trajectories. The present ten methods include: (i) the Ganyu/Shugan doctrine, which regulates mood, circulation, digestion, and reproduction [29], aligning with modern epidemiological brain-cardiovascular-gastroenteric models of depression [29] as a shared pathophysiology—a mechanism previously unrecognized [8, 10, 16, 29, 55–57]. (ii) the most commonly used single-disease model, i.e., the conventional AFS rat model showing substantial depressive-like behavior [30–34], which serves as a comparative reference for the current non-random multimorbidity clusters [58, 59]; (iii) a study design that from bottom to up, opposite one is from up (T cells with dysfunctional mitochondria as first indicator) to bottom (metabolic, cognitive, physical, and cardiovascular multimorbidity) [60]; (iv) an approach in which clusters are treated as equal and homogeneous single-disease components without predefined bias of main and assistant diseases, whereas comorbid bias is sure [61]; (v) no component within the multimorbidity clusters should be overlooked—for instance, poor appetite and its association with reduced gastric emptying, which is a refractory root cause of depression-related coronary events [21]; (vi) the use of raw modeling, drug (herbal), and phytochemical normalization increments (RM/D/PNI), which quantitatively anchors post-AFS 1 h B_1C to 24 h B_2GE five-disease cluster modeling across systems, organs, and spatiotemporal scales [40–43]—facilitated by 21 circulatory biochemical molecules that serve as regulatory intersections within the clusters; (vii) following docking epidemiological conclusions in which invalid or worse depressed cardiac events by antidepressant use with poor appetite as its refractory root cause [21, 23, 45], we reordered the importance from single-disease B_1C B_2GE mrni values (B_2 1.17 > B_1 0.85 > C 0.49 > G 0.36 > E 0.32) to their integration with epidemiological conclusion of pathogenetic mrni [GGB (gastric emptying 0.36-Ghr 0.524-butyrate-14.95) as representative G 15.31 > B_2 1.17 > B_1 0.85 > C 0.49 > E 0.32]; such across-B_1CB_2GE five disease is similar to the comparison between electromyography and gait following normalization [43] (Figure 1).

To avoid false responses from experiments irrelevant to S, mrni-, drni-, prni-, and CR-based normalization analyses were applied, and the detailed equations are provided in the Materials and methods section. Compared with the popular (D − V)/V method [62], which has been widely criticized [32–34], and the direct ACs/herbs comparison approach [13], this strategy markedly reduced false responses (Figures 1 and 2). The present mrni values of eNOS (0.249) and G-emptying (0.36) predicted each other by 69.17%, docking epidemiological eNOS-cardiac event and poor appetite of refractory root [21, 23, 27, 28].

On this basis, the following points further summarize the methodological, phenotypic, and mechanistic implications of the present findings. (viii) Identification of non-random, shared post-AFS stress risks observed consistently over the past 14 years [3, 6–11, 16, 17]. (ix) Temporal 1 h ↑ depressive behavior and ↓ CF, 24 h ↑↑ depressive behavior, ↓ gastric emptying and ↓ enteric transit in AFS rats with B_1CB_2GE of five disease clusters are accurately anchored by Shugan-like CSS/MH-induced, time-to-time, same as above, ↑ antidepressants, ↑ CF, ↑↑ antidepressants, and ↑ gastroenteric prokinetic. There have been no reports on the consistency of organ-to-organ and time-to-time clustering in holistic, including an entity of five functional pharmacological treatments precisely against B_1CB_2GE five diseases; moreover, it is also a future research direction in an authoritative review of *Nature*. (x) Ghr emerged as a shared mechanistic driver. Its pluripotency and the potency of its inhibitor (D-Lys) successfully abolished MH-induced multifunction anchoring of the five-disease B_1CB_2GE cluster in AFS rats, outperforming endothelial-, oxidative-, and inflammation-related mechanisms.

Abbreviations

5-HT: 5-hydroxytryptamine

Ach: acetylcholine

ACs: absorbed compounds

AFS: acute forced swimming

AGEV: antidepressive-gastroenteric prokinetic-vasoactive

B_1CB_2GE: brain$_1$-coronary-brain$_2$-gastro-enteric

BAP: bioethnopharmaceutical analytical pharmacology

BAPevive: bioethnopharmaceutical analytical pharmacology: ex vivo to in vivo

BDNF: brain-derived neurotrophic factor

BMEC: brain microvascular endothelial cells

BS: blank serum

BSS: *Bupleurum chinense* Shugan-San

CFMD: coronary flow-mediated dilation

CR: contribution rate

DG: dentate gyrus

E+: endothelium-dependent

eNOS: endothelial nitric oxide

ET-1: endothelin-1

FA: ferulic acid

FBS: fetal bovine serum

FLX: fluoxetine

FST: forced swimming test

Ghr: ghrelin

H-ECs: H_2O_2-treated endothelial cells

HM: hippocampal microglia

HN: hippocampal neurons

IL-6: interleukin-6

IT: intestinal transit

K-H: Krebs-Henseleit

LH: Lianhuaqingwen

MCP-1: monocyte chemoattractant protein-1

MH: meranzin hydrate

MOS: mosapride

mrni: model raw normalization increment

NO: nitric oxide

NVU: neurovascular unit

OEI: oxidative, endothelial, and inflammatory

PRS: post-dose rat serum

PSDS: post-dose supernatant of deproteinized serum

RAECs: rat aortic endothelial cells

RD: rate of deviation

ROS: reactive oxygen species

S: Sham

SRN: super-regulation network

V: Vehicle

VTI: velocity-time integrals

Supplementary materials

The supplementary materials for this article are available at: https://www.explorationpub.com/uploads/Article/file/1004159_sup_1.pdf.

Declarations

Author contributions

XH: Conceptualization, Resources, Writing—original draft, Writing—review & editing. RZ: Writing—review & editing, Writing—original draft, Methodology, Investigation, Formal analysis, Data curation. CX: Software, Formal analysis, Data curation. HQ: Investigation, Formal analysis, Data curation. YH: Investigation, Formal analysis, Data curation. ZG and QZ: Formal analysis, Data curation. MX, SS, AY, JZ, YL, and CS: Validation, Resources, Data curation. PR: Methodology, Investigation. All authors read and approved the submitted version.

Conflicts of interest

All authors declare that they have no known conflict of interest or personal relationships that could have appeared to influence the work reported in this paper.

Ethical approval

All animals in this experiment complied with the ethical rules for experimental animals of Nanjing University of Traditional Chinese Medicine (Number: 201912A008).

Consent to participate

Not applicable.

Consent to publication

Not applicable.

Availability of data and materials

The datasets supporting the findings of this study are available from the corresponding author upon reasonable request.

Funding

Our Research Project was fully supported by the National Natural Science Foundation of China (Grant Nos. 81973589, 81573797, and 81872967). The funders had no role in study design, data collection and analysis, decision to publish, or preparation of the manuscript.

Publisher's note

References

1. Huang X, Qin F, Zhang HM, Xiao HB, Wang LX, Zhang XY, et al. Cardioprotection by Guanxin II in rats with acute myocardial infarction is related to its three compounds. J Ethnopharmacol. 2009;121: 268–73. [DOI] [PubMed]
2. Huang X, Fan R, Zhang H, Ren P, Qing F, Wang Y. Bioethnopharmaceutical analytical pharmacology: a strategy for elucidating ethnoherbal absorbed bioactive compounds. Chin Tradit Herb Drugs. 2010; 41:337–9.
3. Shi S, Yan H, Chen Y, Liu Y, Zhang X, Xie Y, et al. Pharmacokinetic study of precisely representative antidepressant, prokinetic, anti-inflammatory and anti-oxidative compounds from Fructus aurantii and Magnolia Bark. Chem Biol Interact. 2020;315:108851. [DOI] [PubMed]
4. Huang X, Zhao Q, Xia L, Shi S. Letter to the Editor in response to the articles 'Lianhuaqingwen exerts anti-viral and anti-inflammatory activities against novel coronavirus (SARS-CoV-2)' and 'Liu Shen capsule shows antiviral and anti-inflammatory abilities against novel coronavirus SARS-CoV-2 via suppression of NF-κB signaling pathway.'. Pharmacol Res. 2021;163:105289. [DOI] [PubMed] [PMC]
5. Huang Y, Xu M, Li J, Chen K, Xia L, Wang W, et al. Ex vivo to in vivo extrapolation of syringic acid and ferulic acid as grape juice proxies for endothelium-dependent vasodilation: Redefining vasoprotective resveratrol of the French paradox. Food Chem. 2021;363:130323. [DOI] [PubMed]
6. Zhang YJ, Huang X, Wang Y, Xie Y, Qiu XJ, Ren P, et al. Ferulic acid-induced anti-depression and prokinetics similar to Chaihu-Shugan-San via polypharmacology. Brain Res Bull. 2011;86:222–8. [DOI] [PubMed]
7. Zhang YJ, Huang W, Huang X, Wang Y, Wang Z, Wang C, et al. Fructus Aurantii induced antidepressant effect via its monoaminergic mechanism and prokinetic action in rat. Phytomedicine. 2012;19: 1101–7. [DOI] [PubMed]
8. Xie Y, Huang X, Hu SY, Qiu XJ, Zhang YJ, Ren P, et al. Meranzin hydrate exhibits anti-depressive and prokinetic-like effects through regulation of the shared α2-adrenoceptor in the brain-gut axis of rats in the forced swimming test. Neuropharmacology. 2013;67:318–25. [DOI] [PubMed]
9. Mu DZ, Xue M, Xu JJ, Hu Y, Chen Y, Ren P, et al. Antidepression and Prokinetic Effects of Paeoniflorin on Rats in the Forced Swimming Test via Polypharmacology. Evid Based Complement Alternat Med. 2020;2020:2153571. [DOI] [PubMed] [PMC]
10. Liu YL, Xu JJ, Han LR, Liu XF, Lin MH, Wang Y, et al. Meranzin Hydrate Improves Depression-Like Behaviors and Hypomotility via Ghrelin and Neurocircuitry. Chin J Integr Med. 2023;29:490–9. [DOI] [PubMed]
11. Luo M, Huang X, Wang Y, Ren P. Zhiqiaochuanxiong decoction for major depressive disorder complicated by functional dyspepsia: a case report with fast-acting efficacy. J Tradit Chin Med. 2015; 35:697–702. [DOI] [PubMed]
12. Zhou RZ, Xu CD, Qian HT, Huang X. Ex vivo to in vivo extrapolation of primary absorbed compounds as multifunctional proxies of Zhiqiao (Fructus Aurantii Submaturus)-Houpo (Cortex Magnoliae Officinalis) herb pair. J Tradit Chin Med. 2026;46:51–61. [DOI] [PubMed]
13. Liu Y, Wang W, Chen Y, Yan H, Wu D, Xu J, et al. Simultaneous quantification of nine components in the plasma of depressed rats after oral administration of Chaihu-Shugan-San by ultra-performance liquid chromatography/quadrupole-time-of-flight mass spectrometry and its application to pharmacokinetic studies. J Pharm Biomed Anal. 2020;186:113310. [DOI] [PubMed]

14. Porsolt RD, Anton G, Blavet N, Jalfre M. Behavioural despair in rats: a new model sensitive to antidepressant treatments. Eur J Pharmacol. 1978;47:379–91. [DOI] [PubMed]
15. De Winter BY, Bredenoord AJ, De Man JG, Moreels TG, Herman AG, Pelckmans PA. Effect of inhibition of inducible nitric oxide synthase and guanylyl cyclase on endotoxin-induced delay in gastric emptying and intestinal transit in mice. Shock. 2002;18:125–31. [DOI] [PubMed]
16. Liu X, Luo M, Wang Z, Yang SJ, Su M, Wang Y, et al. Mind shift I: Fructus Aurantii - Rhizoma Chuanxiong synergistically anchors stress-induced depression-like behaviours and gastrointestinal dysmotility cluster by regulating psycho-immune-neuroendocrine network. Phytomedicine. 2024;128:155324. [DOI] [PubMed]
17. Zhao Q, Liu J, Chen L, Gao Z, Lin M, Wang Y, et al. Phytomedicine Fructus Aurantii-derived two absorbed compounds unlock antidepressant and prokinetic multi-functions via modulating 5-HT3/GHSR. J Ethnopharmacol. 2024;323:117703. [DOI] [PubMed]
18. Fujitsuka N, Asakawa A, Hayashi M, Sameshima M, Amitani H, Kojima S, et al. Selective serotonin reuptake inhibitors modify physiological gastrointestinal motor activities via 5-HT2c receptor and acyl ghrelin. Biol Psychiatry. 2009;65:748–59. [DOI] [PubMed]
19. Gastaldon C, Raschi E, Kane JM, Barbui C, Schoretsanitis G. Post-Marketing Safety Concerns with Esketamine: A Disproportionality Analysis of Spontaneous Reports Submitted to the FDA Adverse Event Reporting System. Psychother Psychosom. 2021;90:41–8. [DOI] [PubMed]
20. Chancellor D. The depression market. Nat Rev Drug Discov. 2011;10:809–10. [DOI] [PubMed]
21. Hawkins MA, Callahan CM, Stump TE, Stewart JC. Depressive symptom clusters as predictors of incident coronary artery disease: a 15-year prospective study. Psychosom Med. 2014;76:38–43. [DOI] [PubMed] [PMC]
22. Afridi MI, Siddiqui MA, Ansari A. Gastrointestinal somatization in males and females with depressive disorder. J Pak Med Assoc. 2009;59:675–9. [PubMed]
23. Norton J, Pastore M, Ancelin M, Hotopf M, Tylee A, Mann A, et al. Time-dependent cognitive and somatic symptoms of depression as predictors of new cardiac-related events in at-risk patients: the UPBEAT-UK cohort. Psychol Med. 2021;51:1271–8. [DOI] [PubMed]
24. Bracken RM, Linnane DM, Brooks S. Plasma catecholamine and nephrine responses to brief intermittent maximal intensity exercise. Amino Acids. 2009;36:209–17. [DOI] [PubMed]
25. Stockhorst U, Antov MI. Modulation of Fear Extinction by Stress, Stress Hormones and Estradiol: A Review. Front Behav Neurosci. 2016;9:359. [DOI] [PubMed] [PMC]
26. Ning B, Wei Y, Luo C, Yang L, Zheng Z, Fang P, et al. Natural products targeting the gut-brain axis for the treatment of post-cardiac procedures anxiety or depression. Phytomedicine. 2026;155:158061. [DOI] [PubMed]
27. Carney RM, Freedland KE. Depression and coronary heart disease. Nat Rev Cardiol. 2017;14:145–55. [DOI] [PubMed]
28. Edmondson D, Newman JD, Whang W, Davidson KW. Emotional triggers in myocardial infarction: do they matter? Eur Heart J. 2013;34:300–6. [DOI] [PubMed] [PMC]
29. Li L, Yu AL, Wang ZL, Chen K, Zheng W, Zhou JJ, et al. Chaihu-Shugan-San and absorbed meranzin hydrate induce anti-atherosclerosis and behavioral improvements in high-fat diet ApoE-/- mice via anti-inflammatory and BDNF-TrkB pathway. Biomed Pharmacother. 2019;115:108893. [DOI] [PubMed]
30. Yin X, Guven N, Dietis N. Stress-based animal models of depression: Do we actually know what we are doing? Brain Res. 2016;1652:30–42. [DOI] [PubMed]
31. Kennedy CLM, Carter SD, Mifsud KR, Reul JMHM. Unexpected effects of metyrapone on corticosteroid receptor interaction with the genome and subsequent gene transcription in the hippocampus of male rats. J Neuroendocrinol. 2020;32:e12820. [DOI] [PubMed]
32. Trunnell ER, Carvalho C. The forced swim test has poor accuracy for identifying novel antidepressants. Drug Discov Today. 2021;26:2898–904. [DOI] [PubMed]

33. Gururajan A, Reif A, Cryan JF, Slattery DA. The future of rodent models in depression research. Nat Rev Neurosci. 2019;20:686–701. [DOI] [PubMed]
34. Reardon S. Rodent tests for psychiatric drugs get a rethink. Science. 2024;383:1279. [DOI] [PubMed]
35. Gagliano G, Monteverdi A, Casali S, Laforenza U, Gandini Wheeler-Kingshott CAM, D'Angelo E, et al. Non-Linear Frequency Dependence of Neurovascular Coupling in the Cerebellar Cortex Implies Vasodilation-Vasoconstriction Competition. Cells. 2022;11:1047. [DOI] [PubMed] [PMC]
36. Huang W, Huang X, Xing Z, Qiu X, Wang Y, Fan R, et al. Meranzin hydrate induces similar effect to Fructus Aurantii on intestinal motility through activation of H1 histamine receptors. J Gastrointest Surg. 2011;15:87–96. [DOI] [PubMed]
37. Wang L, Zhou GB, Liu P, Song JH, Liang Y, Yan XJ, et al. Dissection of mechanisms of Chinese medicinal formula Realgar-Indigo naturalis as an effective treatment for promyelocytic leukemia. Proc Natl Acad Sci. 2008;105:4826–31. [DOI]
38. Salewskij K, Penninger JM. Blood Vessel Organoids for Development and Disease. Circ Res. 2023;132: 498–510. [DOI] [PubMed]
39. König P, Dedio J, Müller-Esterl W, Kummer W. Distribution of the novel eNOS-interacting protein NOSIP in the liver, pancreas, and gastrointestinal tract of the rat. Gastroenterology. 2002;123:314–24. [DOI] [PubMed]
40. Schaum N, Lehallier B, Hahn O, Pálovics R, Hosseinzadeh S, Lee SE, et al.; Tabula Muris Consortium; Pisco AO, Karkanias J, Neff NF, Keller A, Darmanis S, Quake SR, et al. Ageing hallmarks exhibit organ-specific temporal signatures. Nature. 2020;583:596–602. [DOI] [PubMed] [PMC]
41. Codarri Deak L, Nicolini V, Hashimoto M, Karagianni M, Schwalie PC, Lauener L, et al. PD-1-cis IL-2R agonism yields better effectors from stem-like CD8+ T cells. Nature. 2022;610:161–72. [DOI] [PubMed] [PMC]
42. Despic V, Jaffrey SR. mRNA ageing shapes the Cap2 methylome in mammalian mRNA. Nature. 2023; 614:358–66. [DOI] [PubMed] [PMC]
43. Kubota K, Yokoyama M, Onitsuka K, Kanemura N. The investigation of an analysis method for co-activation of knee osteoarthritis utilizing normalization of peak dynamic method. Gait Posture. 2023; 101:48–54. [DOI] [PubMed]
44. Han M, Zeng D, Tan W, Chen X, Bai S, Wu Q, et al. Brain region-specific roles of brain-derived neurotrophic factor in social stress-induced depressive-like behavior. Neural Regen Res. 2025;20: 159–73. [DOI] [PubMed] [PMC]
45. Vaccarino V, Badimon L, Bremner JD, Cenko E, Cubedo J, Dorobantu M, et al.; ESC Scientific Document Group Reviewers. Depression and coronary heart disease: 2018 position paper of the ESC working group on coronary pathophysiology and microcirculation. Eur Heart J. 2020;41:1687–96. [DOI] [PubMed] [PMC]
46. Greaney JL, Saunders EFH, Santhanam L, Alexander LM. Oxidative Stress Contributes to Microvascular Endothelial Dysfunction in Men and Women With Major Depressive Disorder. Circ Res. 2019;124: 564–74. [DOI] [PubMed] [PMC]
47. Stone LA, Harmatz ES, Goosens KA. Ghrelin as a Stress Hormone: Implications for Psychiatric Illness. Biol Psychiatry. 2020;88:531–40. [DOI]
48. Elantary R, Othman S. Role of L-carnitine in Cardiovascular Health: Literature Review. Cureus. 2024; 16:e70279. [DOI]
49. Wang Z, Wu F, Zhou Q, Qiu Y, Zhang J, Tu Q, et al. Berberine Improves Vascular Dysfunction by Inhibiting Trimethylamine-N-oxide via Regulating the Gut Microbiota in Angiotensin II-Induced Hypertensive Mice. Front Microbiol. 2022;13:814855. [DOI] [PubMed] [PMC]
50. Xie A, Ensink E, Li P, Gordevičius J, Marshall LL, George S, et al. Bacterial Butyrate in Parkinson's Disease Is Linked to Epigenetic Changes and Depressive Symptoms. Mov Disord. 2022;37:1644–53. [DOI] [PubMed] [PMC]

51. Procházková N, Falony G, Dragsted LO, Licht TR, Raes J, Roager HM. Advancing human gut microbiota research by considering gut transit time. Gut. 2023;72:180–91. [DOI] [PubMed] [PMC]
52. Llorens-Martín M, Jurado-Arjona J, Bolós M, Pallas-Bazarra N, Ávila J. Forced swimming sabotages the morphological and synaptic maturation of newborn granule neurons and triggers a unique pro-inflammatory milieu in the hippocampus. Brain Behav Immun. 2016;53:242–54. [DOI] [PubMed]
53. Musazzi L, Tornese P, Sala N, Popoli M. Acute or Chronic? A Stressful Question. Trends Neurosci. 2017; 40:525–35. [DOI] [PubMed]
54. Müller TD, Nogueiras R, Andermann ML, Andrews ZB, Anker SD, Argente J, et al. Ghrelin. Mol Metab. 2015;4:437–60. [DOI] [PubMed] [PMC]
55. Whitty CJM, Watt FM. Map clusters of diseases to tackle multimorbidity. Nature. 2020;579:494–6. [DOI] [PubMed]
56. Pietzner M, Stewart ID, Raffler J, Khaw KT, Michelotti GA, Kastenmüller G, et al. Plasma metabolites to profile pathways in noncommunicable disease multimorbidity. Nat Med. 2021;27:471–9. [DOI] [PubMed] [PMC]
57. Whitney DG, Schmidt M, Hurvitz EA. Shared Physiologic Pathways Among Comorbidities for Adults With Cerebral Palsy. Front Neurol. 2021;12:742179. [DOI] [PubMed] [PMC]
58. Shabir O, Moll TA, Matuszyk MM, Eyre B, Dake MD, Berwick J, et al. Preclinical models of disease and multimorbidity with focus upon cardiovascular disease and dementia. Mech Ageing Dev. 2020;192: 111361. [DOI] [PubMed]
59. Claypool AL, Goldhaber-Fiebert JD, Brandeau ML. Assessing Interventions That Prevent Multiple Infectious Diseases: Simple Methods for Multidisease Modeling. Med Decis Making. 2022;42:436–49. [DOI] [PubMed] [PMC]
60. Desdín-Micó G, Soto-Heredero G, Aranda JF, Oller J, Carrasco E, Gabandé-Rodríguez E, et al. T cells with dysfunctional mitochondria induce multimorbidity and premature senescence. Science. 2020; 368:1371–6. [DOI] [PubMed] [PMC]
61. Skou ST, Mair FS, Fortin M, Guthrie B, Nunes BP, Miranda JJ, et al. Multimorbidity. Nat Rev Dis Primers. 2022;8:48. [DOI]
62. Yang Y, Cui Y, Sang K, Dong Y, Ni Z, Ma S, et al. Ketamine blocks bursting in the lateral habenula to rapidly relieve depression. Nature. 2018;554:317–22. [DOI] [PubMed]